JPRS Report

Science & Technology

Japan

NEW FUNCTIONAL CERAMICS SEMINAR

DTIC QUALITY INSPECTED 2

19980507 127

SCIENCE & TECHNOLOGY
JAPAN

NEW FUNCTIONAL CERAMICS SEMINAR

[Selected papers from the 19th New Ceramics Seminar on New Functional Ceramics held 2-3 Mar 92 in Osaka, sponsored by the New Ceramics Forum and Osaka Prefectural Technology Association]

Contents

Development of ZnSe Blue LED by MBE

[Article by Tsuneo Mitsuro and Kazuhiro Okawa, Central Research Laboratory, Matsushita Electric Industrial Co., Ltd.]

[Text] 1. **Introduction**

Light-emitting diodes (LED) currently in commercial use produce visible light of wavelengths ranging from the red to green light range. Efforts have been under way to develop LEDs generating a shorter-wavelength blue light. Successful development of these diodes will increase the variety of LED colors available and will make it possible to produce LED display units capable of rendering a full-color range of visible light. The development of blue color-emitting LEDs will also contribute to the development of superhigh-density optical disk memory devices by promoting the development of blue-light laser diodes (LDs) by taking advantage of the diode's short wavelength. Last year, a report disclosed a success in generating bluish-green pulse-oscillation light using CdZnSe-system semiconductor devices.

Semiconductors for generating blue-light LEDs must have the forbidden bands wider than about 2.6 eV. As candidate semiconductors, ZnSe and ZnS, as the II-VI group compounds, and SiC and GaN are being studied. Among them, research on SiC and GaN has progressed to a point where sample shipments of these LEDs has started. However, these LEDs must be refined further before they can be used in practical applications. SiC makes it possible to create the pn junction necessary to produce a high degree of luminescence relatively easily. Its drawback is that the material efficiency rate is difficult to increase substantially because it is an indirect transition semiconductor. Therefore, it is believed that SiC is not suitable for use in developing laser diodes.

In GaN, it is very difficult to create p-type crystals, though the material is a direct-transition semiconductor. Because of this, the only LED that has been developed is the MIS type in which the device is fabricated by forming electrodes on the n-type crystal substrate via an insulation layer. In this type of LED, the light-emission rate cannot be increased easily. These II-VI group materials are all direct-transition semiconductors. In these semiconductors, practically usable p-type elements have not been attained yet.

A reason for this difficulty is believed to be self-compensatory effects in these semiconductors cause the generation of doners attributed to the presence of the point defects, even if acceptor impurities are introduced into them. The adoption of nonthermal equilibrium (low-temperature) crystal growth methods is believed to solve this problem. Under these circumstances, low-temperature crystal-film growth methods, through molecular beam epitaxy (MBE) and metallo-organic chemical vapor deposition (MOCVD) are attracting increasing attention in recent years. Active efforts to realize epitaxial growth and controlling electric conductivity in ZnSe and other II-VI group-compound semiconductors have been made. These efforts have made it possible to create p-type crystals. Such crystallized semiconductors were used to develop the LD capable of generating bluish green laser light, as mentioned above. However, there are still many problems that must be solved before producing practically usable LED elements.

We have conducted research to promote epitaxial growth in ZnSe by the MBE method. Research involved the use of a proprietary impurity introduction technology to control electric conductivity to obtain low-resistance n-type and p-type ZnSe. The research also involved experimental fabrication of pn junction LEDs. In the following, we will describe the technique to grow ZnSe crystal by the MBE method and the electric and optical characteristics of n-type as well as p-type crystals. Though they are still at the rudimentary technological level, the results of measurement of the characteristics of the pn junction LEDs will also be introduced.

2. ZnSe Growth by MBE Method

Figure 1 shows the outline of the crystal-growing chamber in the MBE apparatus. By using this apparatus, a thin film single crystal of SnSe can be formed on the surface of a heated substrate by irradiating it with a Zn molecular beam and an Se molecular beam. These beams are generated by the resistor-heated Knudsen cell (K cell) crucibles within a vacuum environment of about 10^{-9} Torr. Commonly, GaAs substrates are used having a lattice constant close to that of the ZnSe (lattice mismatch: 0.25%) Our research used GaAs substrates and more ideal Se
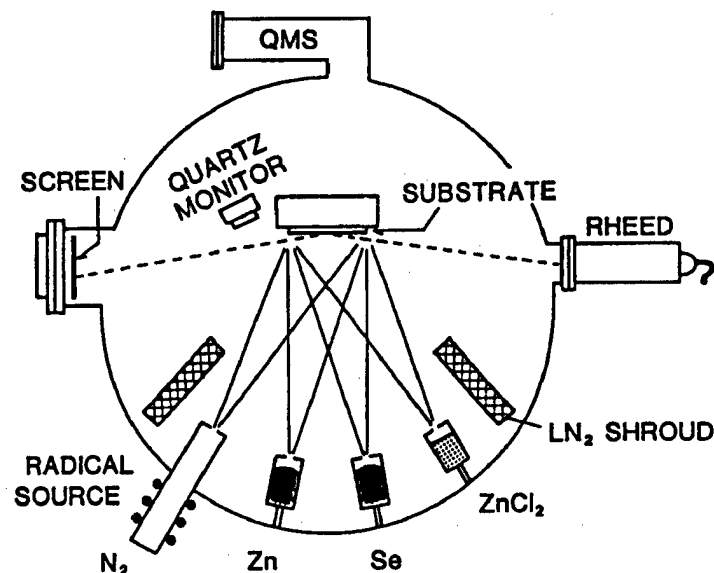
Figure 1. Schematic Representation of MBE Apparatus Reaction Chamber

bulk substrates to test the homoepitaxial growth. In the bulk-crystal substrates, it is difficult to remove the deteriorated surface layer caused by the processing. We have obtained good results by applying a reactive ion dry etching using BCl_3 gas. Commonly, the crystal growth is carried out under a molecular beam strength ratio between Zn and Se of 1:1, and a growth speed of

2

about 1 μm/h by maintaining the substrate temperature between 300–350°C. An n–type ZnSe crystal layer can be grown by irradiating the substrate with a $ZnCl_2$ molecular beam in addition to irradiation with Zn and Se molecular beams to carry out a Cl doping of the growth film. A p–type ZnSe crystal layer can be formed by irradiating the substrate with a neutral, high–frequency discharge–excited active nitrogen molecular beam. The technology involved in these doping operations will be elaborated on in later sections of this paper.

The evaluation of the MBE grown, additive–free ZnSe crystalline condition by using the half–value width of the X–ray diffraction rocking curves showed that in the case of using GaAs substrates, the half–value width of about 100 seconds was obtained for a film about 5 μm in thickness. The crystalline condition varied with the change in thickness of the crystallized film because of the presence of a lattice mismatch. In the case of ZnSe substrates,

Figure 2. Low–Temperature PL Spectrum in No–Additive–Containing ZnSe

excellent results have been obtained with a maximum half–value width of about 20 seconds. The width changed depending on the crystalline condition. Figure 2 shows the low–temperature photoluminescence spectrum of the no impurity–containing ZnSe film formed on a GaAs substrate. The spectrum is dominated by the peaks occurring near the ends of the spectrum band representing the luminescence caused by free excitons. The luminescence attributed to impurity contents and the structural defects is weak. This indicates that a high–purity crystal having low defects has been created. However, closer study revealed that the splits in exciton luminescence and the energy shifts had occurred as a result of the presence of a mismatch in the lattice constants and the occurrence of lattice deformations because of a mismatch in the thermal expansion coefficients. ZnSe substrates are free from these problems, making it possible to grow crystal under better growth conditions. Electric resistance in these ZnSe substrates containing no additives was measured at values higher than 10^4 $\Omega\cdot$cm, indicating that the crystal films formed on these substrates have very low levels of residual doners and high purities.

3. Cl-Doped N-Type ZnSe

Used as n–type impurities to create n–type ZnSe, the III group elements, such as Al, Ga, and In, have been used popularly to produce doners by causing the replacements at the Zn sites. However, the carrier density obtained by these replacements is no higher than 10^{17}/cm^3, a level insufficient to produce
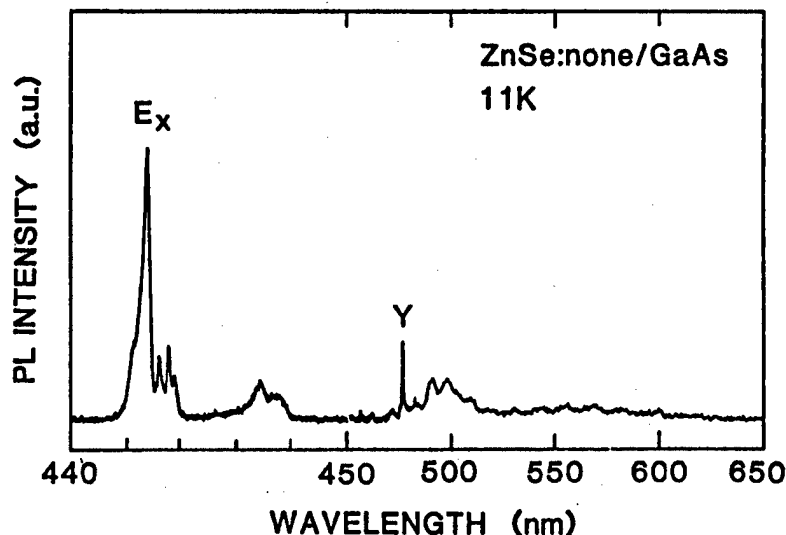
practically usable LEDs. So, we adopted
Cl as a VII group element to promote the
replacements at the Se sites. Since Cl_2
and HCl gas, the materials to produce
Cl, cause damage to the MBE apparatus,
solid $ZnCl_2$ has been used in our re-
search. $ZnCl_2$ sublimates easily. It is
believed that this makes Cl reach the
substrate surface in a molecular form.

Figure 3 illustrates the relationship
between the electric characteristics
(carrier density, mobility μ, resistivi-
ty ρ) in Cl-doped ZnSe and the tempera-
ture change in the $ZnCl_2$ cell. With
increased cell temperature, the carrier
density rises to a maximum of $10^{19}/cm^3$.
The value of ρ also increases to reach
the 10^{-3} $\Omega \cdot cm$ level. The carrier density
curve almost overlaps the Cl vapor-
pressure curve, indicating that Cl is
taken into the crystal effectively as an
impurity. The reason for this high effi-
ciency is believed to be attributed to
the active nature of Cl ions.

Figure 3. Electric Characteristics
in Cl-Doped n-Type ZnSe
(Effect of $ZnCl_2$ cell temperature)

Figure 4 shows the room temperature PL
spectra for no-impurity-containing
ZnSe and its Cl-doped counterpart.
When no additive is introduced, a
weak luminescence is observed at a
wavelength of 460 nm near the low end
of the spectrum (the magnification
rate in the axis of ordinate is given
on the right side of the graph). Cl-
doped ZnSe grown under a cell temper-
ature of 200°C exhibits a lumines-
cence intensity about three digits
higher than the no-additive counter-
part at the band-end wavelength. This
improvement is believed to have been
caused as a result of recombination
between the doner electrons and free
holes. This also suggests that Cl was
effectively taken into ZnSe to func-

Figure 4. Room Temperature PL Spectra
for No-Additive-Containing Cl-Doped
ZnSe Crystals

tion as doners. When the Cl concentration increases further as a result of an
increase in cell temperature, the longer-wavelength luminescence resulting
from the appearance of compound defects caused by the high density of Cl and
the vacancies becomes dominant. However, such defects do not constitute a
major problem in practical applications because the formation of electrode
contact layers is the only process in which such a high-level doping becomes
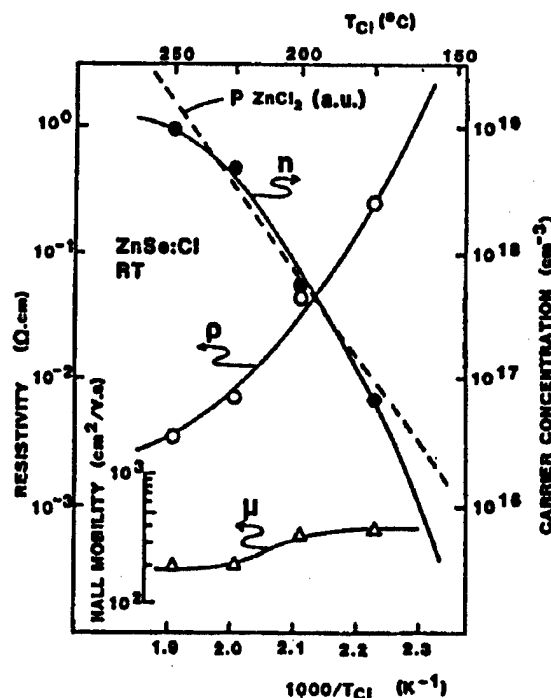necessary.

4

4. N-Doped, P-Type ZnSe

As candidate p-type impurities to produce p-type ZnSe, there are Li and Na as the I group elements, and N, P, and As, as the V group elements. Among these, Li was the first to be tested as a p-type impurity. However, considering its very high diffusivity, it would be difficult to use it in producing practically usable pn junction elements. For the same reason, Na, too, would not be suitable. P and As are reported to form deep impurity levels easily, and this would make it difficult to attain high-density doping. Under the circumstances, we tested N by supplying N_2 and NH_3 gases in growing a ZnSe crystal. The results indicated that in growing the crystal by the MBE method, the level of these elements taken into ZnSe was very low because of their low reactivity. In an effort to enhance the reactivity, we tested a method that involved irradiating the substrate with a low-energy nitrogen ion beam (about 100 eV). The result was that N was taken into function as an acceptor at the shallow depth of the crystal (from the study of the PL characteristics). However, an increase of the doping level led to aggravation of the crystallization because of ion-caused damages, making it impossible to obtain p-type ZnSe crystals.

Next, we tried a method entailing the use of neutral excitons to enhance the activity of the ions without causing damage. The method involved exciting nitrogen gas with a high-frequency electrodeless discharge, and generating neutral particles by using a specially-designed MBE gun (Figure 1). An N doping using an MBE apparatus equipped with the gun produced a ZnSe crystal exhibiting p-type conductivity. Figure 5 shows the low-temperature PL spectra for two types of ZnSe having different N-doping levels. The spectrum (a) is representative of a ZnSe having an N density lower than $10^{-17}/cm^3$. The spectrum is dominated by I_1 line luminescence, the luminescence caused by the excitons restrained by neutral acceptors. A weaker luminescence caused by the doner-acceptor pair (DAP) is also observed. From the wavelengths of these luminescence peaks, the ionization energy of the acceptor was calculated at about 110 meV. This coincided well with the value reported by other researchers, indicating that N replaces the Se to form shallow-depth acceptors. The ZnSe specimens we have created had a comparatively high electrical resistance, indicating the necessity to increase the acceptor
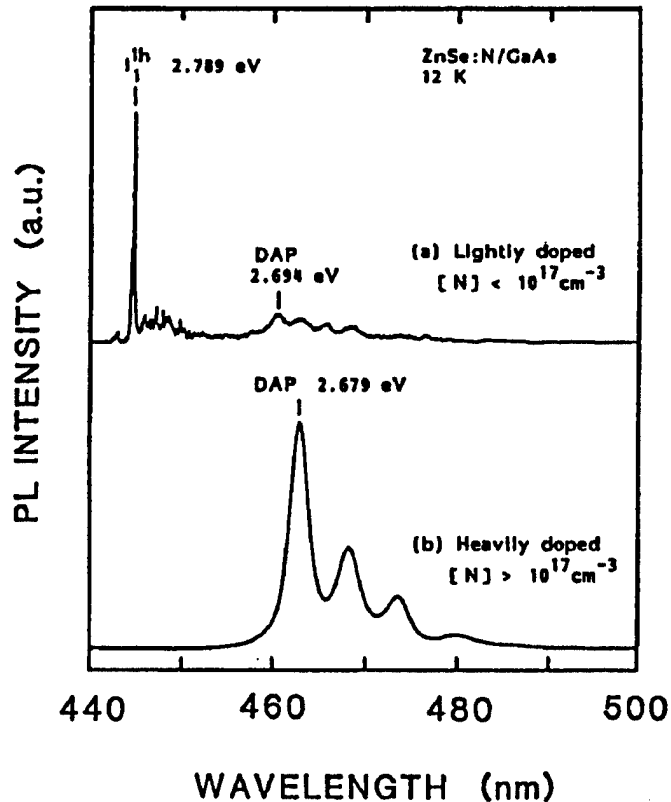

Figure 5. Low-Temperature PL Spectra for Activated N-Doped ZnSe

density further. Further increase of N density caused the disappearance of exciton luminescence (Figure 5(b)) and an increase in the intensity of DAP luminescence. Measurement of the hall effects confirmed the presence of a p-type conduction.

Figure 6 illustrates the relationships between doped N concentration level and the DAP luminescence intensity with the data obtained by secondary ion mass spectroscopy (SIMS) analysis. A p-type conduction was obtained between N concentration levels of about $1\sim3\times10^{18}$/cm^3 in which intense DAP luminescence was observed. The room temperature carrier density, obtained by the hall effect measurement, ranged from about $10^{15}\sim10^{17}$/cm^3. These values indicate that the activation rate is still considerably low even when the large ionization energy of the acceptor was taken into account. This suggests that compensation by the doner is taking place, and it is indicated by the fact that the PL characteristics are dominated by DAP luminescence. How the doners are formed is not known yet. It is believed that they are created either by impurities finding their way into ZnSe crystal from active nitrogen sources, or by the vacancies, or by nitrogen atoms that failed to displace the Se. To solve this problem, it is important to further improve crystal growth conditions.

Figure 7 shows the relationships between the carrier density in N-doped p-type ZnSe and the hole mobility. Maximum dielectric constant reaches 2×10^{17}/cm^3 with mobility deteriorating markedly when the density increases. It is believed that this has something to do with the doner's compensation effects.
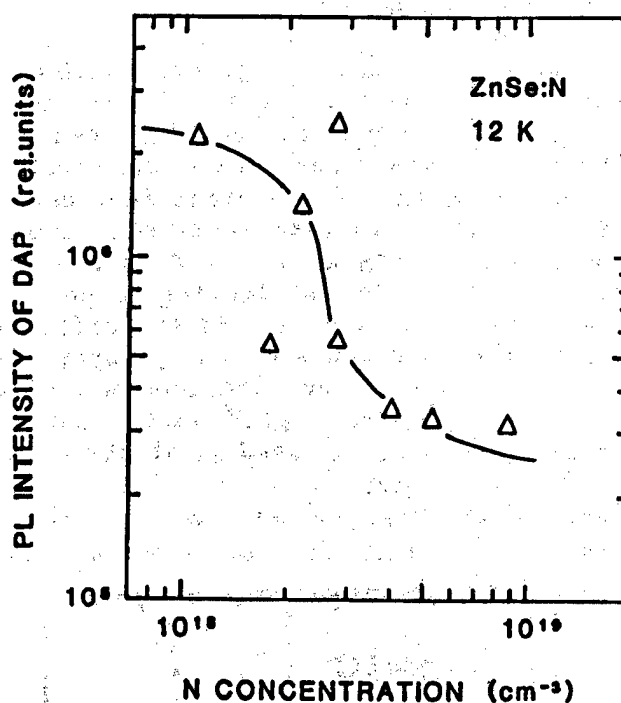

Figure 6. Relationships Between Doped N Density and DAP Luminescence Intensity With Data Obtained by SIMS Analysis
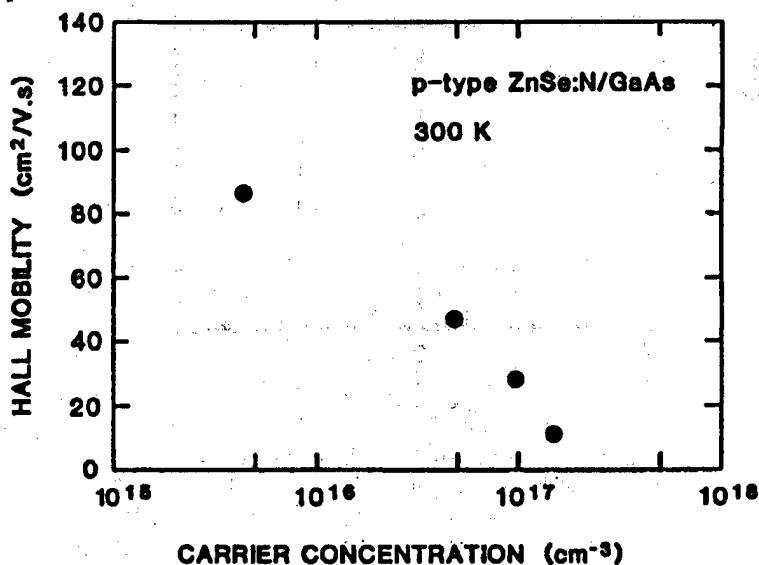

Figure 7. Relationships Between Carrier Density and Hole Mobility in N-Doped p-Type ZnSe

5. PN Junction LEDs

We have fabricated pn junction LEDs on an experimental basis using the above techniques for growing n-type as well as p-type ZnSe crystals. Figure 8 represents the construction of such a pn junction element fabricated on a ZnSe substrate. We also fabricated a pn junction element using an n-type GaAs substrate. A major obstacle in fabricating a pn junction element on ZnSe substrate is the difficulty in forming the electrodes on the p layer. Commonly, Au is used as the electrode material; the problem is to create good ohmic contacts. In our experiment Pt was used as electrode material. Pt is believed to be superior to Au. The adoption of this process made it possible to slightly alleviate the ohmic-contact problem.
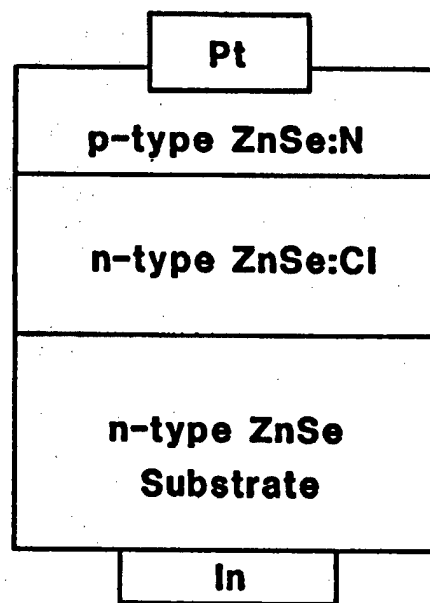
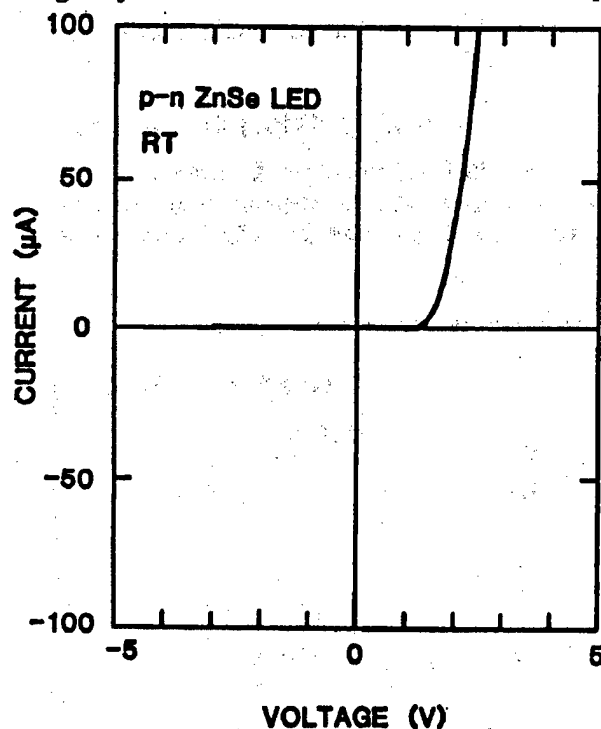Figure 8. Construction in Fabricated pn-Junction LEDs

Figure 9 shows the I-V characteristics in the fabricated LEDs displaying an excellent pn junction rectification ability. Figure 10 shows the luminescence spectra for the fabricated ZnSe as well as GaAs LEDs at different measurement temperatures. At 77 K, a luminescence (FA) caused by the recombination between the free electrons and hole acceptor levels becomes dominant in both types of LEDs. When the temperature increases, FA luminescence declines and a luminescence (DF) caused by recombination between the doner electrons and free holes replaces FA luminescence. At room temperature, the intensity of DF luminescence was high and the intensity of longer wavelength luminescence was far weaker in the ZnSe LEDs, causing them to produce a quasi-blue luminescence. The luminescence peak appeared at a wavelength of about 460 nm and the half value width is narrow with the width standing at 49 meV. In the GaAs LEDs, the intensity of blue luminescence was very weak and the spectrum was dominated by longer-wavelength luminescences. This difference is believed to have resulted from different crystallization conditions, as described above.

Figure 9. I-V Characteristics in pn-Junction LEDs
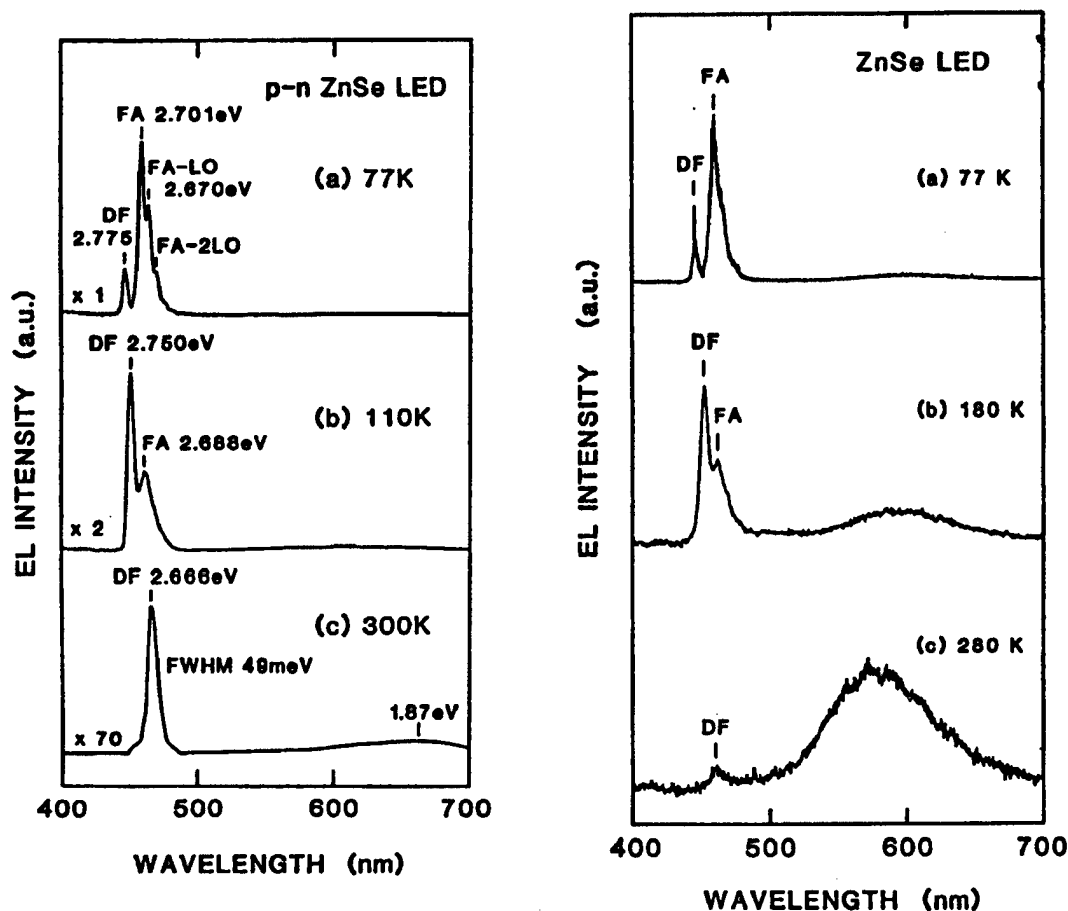
Figure 10. Luminescence Spectra for pn-Junction LEDs
(Left: ZnSe substrates, right: GaAs substrates)

The results obtained from the experimental fabrication of these LEDs are still in their elementary stages, hence discussion of their performance including luminescence would be premature.

6. Summary

We succeeded in creating pn junction LEDs generating a quasi-blue luminescence by developing Cl-doped n-type, low-electric-resistance ZnSe. We activated N-doped p-type ZnSe by the MBE method. Some of the techniques and methods used in our research were used by 3M of the United States, which succeeded in developing bluish-green luminescence LDs last year. These techniques and methods will continue to be used in fabricating ZnSe-system light-emitting devices. To promote the development of practically usable LEDs and LDs, efforts must be continued to promote the improvement of p-layer characteristics, the development of better ohmic-contact electrodes, and the structural optimization in these devices.

Fabrication of Dielectric Thin Film by Sol-Gel Method

[Article by Shinichi Hirano, Nagoya Institute of Technology]

[Text] 1. Introduction

Active research has been under way to develop a technology for synthesizing ferroelectric thin films and evaluating them for application to nonvolatile memories, capacitors, pyroelectric detectors, sensors, and optical modulation elements. To synthesize the films, a number of methods have been used, including the liquid epitaxial phase (LPE), chemical vapor deposition method (CVD), molecular beam epitaxial growth method (MBE), sputtering method, laser abrasion method, and sol-gel method. In recent years, the reduction of the dimensions of electronic devices including various functional elements has made remarkable progress. In addition, efforts for hybridization and improvement of circuit integration are continuing. In order to promote the integration of required functions, the development of a low-temperature synthesizing technology is essential to produce crystallographically preferentially oriented thin films. To promote the required characteristics, the capability to control the chemical composition is indispensable.

Among these methods, the sol-gel method is most preferred because it is comparatively easy to realize high-accuracy chemical-composition controlling, to achieve high homogeneity, to improve purity, to lower the process temperature, and to mold into a desired shape.

Table 1 gives the types of the ferroelectric films developed by this author's team by the sol-gel method using metal alkoxide precursors and the application fields of these films.

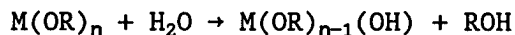This author has found that it is possible to synthesize an epitaxially grown stoichiometric $LiNbO_3$ film at temperatures lower than 400°C by controlling the metal alkoxide reaction process. This paper will describe the processes for synthesizing $LiNbO_3$, $LiNbO_3/Ti$, $Pb(Zr,Ti)O_3$, and $Pb(Mg,Nb)O_3$, some of the typical ferroelectric thin films developed at this author's lab, and the crystallization controlling technique.

9

Table 1. Ferroelectric Thin Films

Thin—film materials	Phenomena	Applications
•Perovskite (Titanates) $BaTiO_3$ $(Ba,Sr)TiO_3$ $SrTiO_3$	Dielectric Pyroelectric PTCR	Capacitors, sensor, phase shifter Pyrodetector Thermistor
$PbTiO_3$ (PT)	Pyroelectric Pyroelectric	Pyrodetector Acoustic transducer
$Pb(Zr,Ti)O_3$ (PZT)	Dielectric Pyroelectric Piezoelectric Electro—optic	Nonvolatile memory Pyrodetector SAW substrate Waveguide device
$(Pb,La)(Zr,Ti)O_3$ (PLZT)	Pyroelectric Electro—optic	Pyrodetector Waveguide device, optical memory, display, SHG
(Niobates) $Pb(Mg_{1/3},Nb_{2/3})O_3$ (PMN) PMN/PT	Dielectric Electro—optic	Capacitor, memory Waveguide device
$LiNbO_3$ (LN) $LiTaO_3$ (LT)	Piezoelectric Electro—optic	Pyrodetector, waveguide device, optical modulator, SAW, SHG
$KNbO_3$ (KN)	Electro—optic	Waveguide device, frequency doubler, holographic storage
$K(Ta,Nb)O_3$ (KTN)	Pyroelectric Electro—optic	Pyrodetector Waveguide device
•Tungsten—Bronze $(Sr,Ba)Nb_2O_6$ (SBN) $(Sr,Ba)_{0.8}RxNa_{0.4}Nb_2O_6$ (R:Cr,Zn,Y) $(Pb,Ba)Nb_2O_6$ (PBN) $(K,Sr)Nb_2O_6$ (KSN) $(Pb,K)Nb_2O_6$ (PKN) $Ba_2NaNb_5O_{15}$ (BNN)	Dielectric Pyroelectric Electro—optic	Memory Pyrodetector Waveguide device

2. Synthesizing Process

Figure 1 is a flow chart of the commonly practiced processes for synthesizing ceramics by the sol-gel method using metal-organic compounds or organometallic compounds. In synthesizing double oxides using plural types of metal alkoxides, the differences of hydrolysis speed in respective alkoxide must be taken into account. The hydrolysis speed in metal alkoxide is dictated by the electronegativity of the metal element, the carbon number in the alkoxide radicals (—OR-), and the conditions in the carbons' three-dimensional structure. Alkoxide radical is a strong Lewis base. It can be hydrolyzed with water easily and produces metallic oxides as hydroxides and alcohol by way of condensed intermediate products as indicated below:

Figure 1. Sol-Gel Processing of Electronic Ceramics

$$M(OR)_n + H_2O \rightarrow M(OR)_{n-1}(OH) + ROH$$

To synthesize double oxides having intended compositions at low temperature, it is important to ensure homogeneity throughout the hydrolysis reaction process. In order to realize this, suitable types of metallic alkoxides must be selected to produce a composite alkoxide to obtain a proper metal-oxygen-metal bonding. The characteristic of the precursor compounds can be controlled through partial hydrolysis of metallic alkoxides. In order to crystallize the gel obtained from the liquid precursor at low temperature by preventing inclusion of free carbon molecules, the crystallization must be carried out within a flowing mixed gas of vaporized water and oxygen rather than by heating within flowing dry oxygen gas.

In forming a homogeneous coating film on the substrate, optimization adjustments will become necessary in the process of chemical bonding of condensated metallic alkoxides within the solution, and in the structure, molecular weight, and wettability between the solution and substrate.

3. Thin Film Synthesizing Process

3.1 Li(Nb,Ta)O₃ Film

Figure 2 is a flow chart of the processes involved in synthesizing an epitaxially grown stoichiometrical $Li(Nb,Ta)O_3$ thin film at temperatures lower than 500°C. The crystal condition and the homogeneity of the chemical composition in the synthesized film are affected by the conditions under which metallic alkoxides dissolved into a solvent are subjected to a refluxing
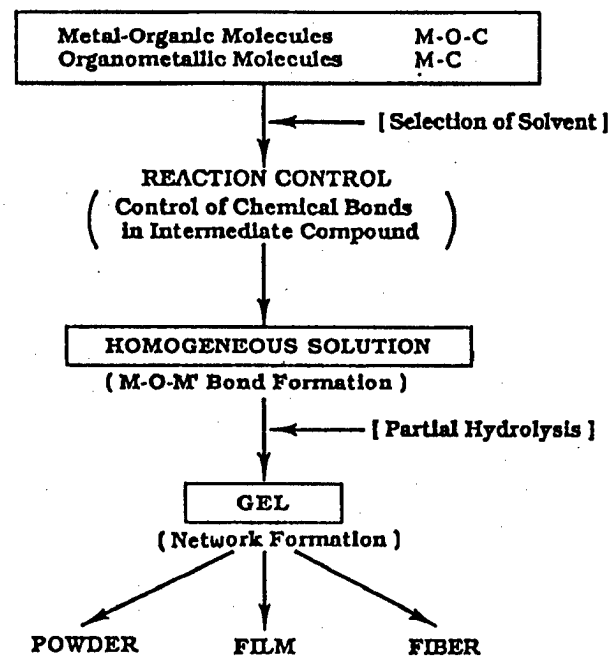
reaction environment. By promoting reactions within the solution, it is possible to synthesize a composite alkoxide, $LiNb(OC_2H_5)_6$. This author's team has studied the solution's reaction process through FT-IR and NMR. Recently, the structure of these intermediate compounds has been reconfirmed by X-ray structural analysis.
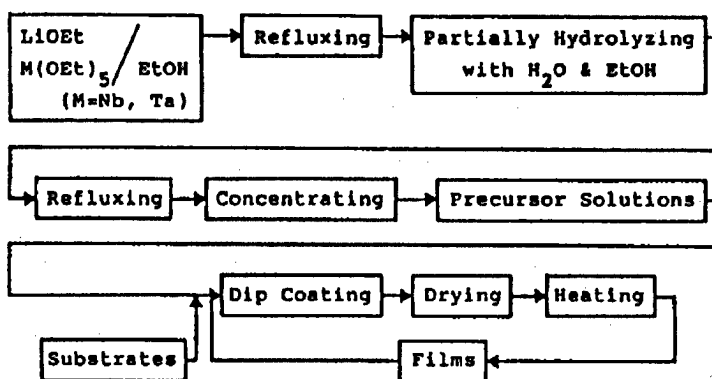

Figure 2. Preparation of Li(Nb,Ta)O_3 Film

The crystal condition in thin film is affected greatly by the volume of water involved in the partial hydrolysis. When synthesizing a thin film by hydrolyzing $LiNb(OC_2H_5)_6$ by adding water, it has been found possible to promote crystallization and to avert the formation of carbon radicals by heating the partially hydrolyzed gel film within a flowing mixed gas of vaporized water and oxygen. By optimizing these conditions, it is possible to synthesize the crystallized thin films on sapphire and Si substrates at temperatures lower than 250°C (Figure 3).

The thickness of the crystal film synthesized in a single dip-coating process depends on the solution density and the speed of pulling up the substrates. When the solution density was kept at the same level, there were straight-line relationships between the log values of the pulling-up speed and the thickness. This makes it easy to obtain a required thickness by repeating the dip-coating process. It has been found that multilayer film thus synthesized has excellent interlayer continuity.

The Li(Nb,Ta)O_3 thin layer synthesized on a sapphire substrate has been found to have a crystal orientation in the same direction as that on the substrate surface. A reflected high-energy electron diffraction (RHEED) observation confirmed that epitaxial crystal growth had taken place.

(a),(b): films heated in a mixed flow of water vapor and oxygen.

(c),(d): films heated in flowing of dry oxygen.

(a),(c): films prepared from solutions with partial hydrolysis.
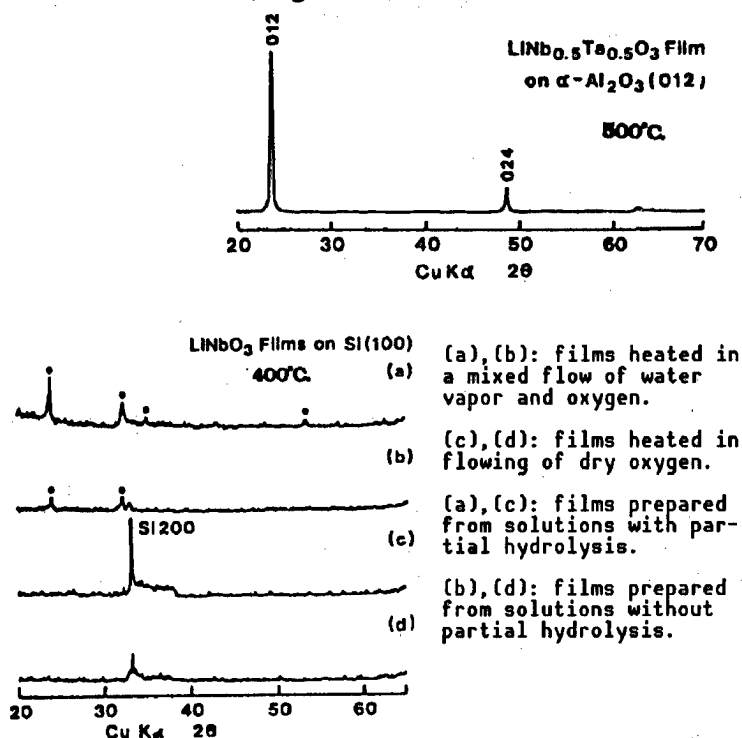
(b),(d): films prepared from solutions without partial hydrolysis.

Figure 3. XRD Profiles of Li(Nb,Ta)O_3 Films

12

In using a thin crystal film to develop electronic devices, the problems of boundary face reactions between the substrate and the film and the mutual dispersion in the boundary region must be taken into account. An Auger electron spectroscopy (AES) analysis and a Rutherford backscattering (RBS) analysis found no problematical mutual scattering between the substrate and the thin film, with the spectra representing Nb and Al atoms showing distinctly sharp profiles.

The $LiNbO_3$ crystal film synthesized on a sapphire substrate at 400°C had a refractive index higher than 2.27 and no granular component was found within the film, that had thick and very smooth texture.

Figure 4 shows the D–E hysteresis loop of an 0.7 μm thick stoichiometrical $LiNbO_3$ thin film synthesized on a Si(111) substrate at 60 Hz. The dielectric constant and other related values of the film were: dielectric constant = 29, Ps = 0.18 $\mu C/cm^2$, Pr = 0.13 $\mu C/cm^2$, Ec = 5.7 kV/cm.

By using the techniques described above, it is possible to synthesize an oriented stoichiometric $LiTaO_3$ film and an $Li(Nb,Ta)O_3$ solid–solution film.

Figure 4. D–E Hysteresis Loop of $LiNbO_3$ Thin Film on Si(111) Substrate at 550°C

3.2 Ti-Doped $LiNbO_3$ Thin Film

In order to use $LiNbO_3$ film as a light–transmitting channel, a study is being conducted to create a light channel by adjusting the refractive index through proton replacement or by diffusing Ti metal into the lattice. However, difficulties are being experienced in controlling the refractive index because of the diffusion coefficients depend on the composition and the defects in $LiNbO_3$ single crystal having a not–right–stoichiometrical composition, and because of density change in replaced ions in the depth direction. In addition, dislocations and cracks occur easily. This author's team has succeeded in forming a solid solution epitaxial film on a sapphire substrate by using a homogeneous solution of $Li(OC_2H_5)$ and $Nb(OC_2H_5)_5$ metal alkoxide by adding up to 5 mol% $Ti(OC_2H_5)_4$. Addition of 5 mol% Ti made it possible to adjust the refractive index in a stoichiometric $LiNbO_3$ film from 2.28~2.50. By further refining this method of channel formation in Ti–doped $LiNbO_3$ film, it would become possible to create light–transmitting channels having sharper channel profiles.

3.3 PZT and PMN Thin Films

In recent years, active research has been conducted to synthesize the thin films of $Pb(Zr,Ti)O_3$ (PZT) and $Pb(Mg,Nb)O_3$ (PMN) ferroelectric substances and to evaluate their characteristics. The properties in the thin films of these ferroelectrics are affected greatly by the presence of a pyrochlore phase. So it is important to promote the formation of a perovskite phase. In general, the formation of a thin film of a perovskite phase on the substrate of silicon or platinum is more difficult than the crystallization of amorphous particles.
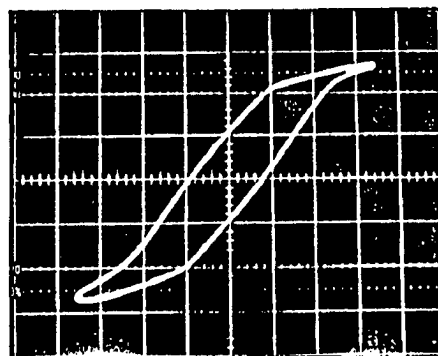
13

On the other hand, on the surface of MgO and SrTiO$_3$ substrates, it is possible to synthesize a perovskite film with its orientation restrained by the crystallized face conditions.

Figure 5 gives the PZT thin film synthesis conditions adopted by this author's team. In order to realize the crystallization of a perovskite figure-phase thin film under low temperature, it is necessary to have Zr positioned at the B sites of the perovskite structure and Ti ions properly configured within the solution prior to subjecting them to reaction with lead acetate anhydride. Lead acetate anhydride can be used effectively to control the reaction. Further, the stability of the precursor solution can be improved with the addition of acetyl acetone. In the crystallization of this compound, it has been found that the calcination of the gel film within the flowing mixed gas of vaporized water and oxygen is very useful for promoting the crystallization of perovskite phase and the synthesis of the oriented film at low temperature.

Figure 5. Processing Conditions of PZT Films

Perovskite thin film is synthesized at temperatures higher than 450°C. Figure 6 shows the X-ray diffraction analysis (XRD) profiles of a crystallized film of Pb(Zr$_{0.53}$Ti$_{0.47}$)O$_3$ film synthesized on a Pt/Ti/SiO$_2$/Si substrate. This film displayed a typical D-E hysteresis and had a dielectric constant of about 600.

It is known that PMN and PT(PbTiO$_3$) form a solid solution between them. To exploit this, effort must be made to control the composition of the thin film to promote the required properties. PMN-system compounds are one of those substances that cannot be crystallized into perovskite phase easily. This poses a great challenge to those who try to produce perovskite PMN films.

Figure 7 gives the processing parameters for synthesizing perovskite PMN/PT films.
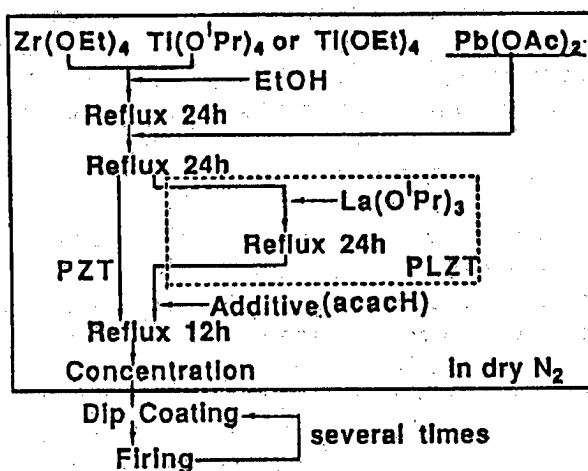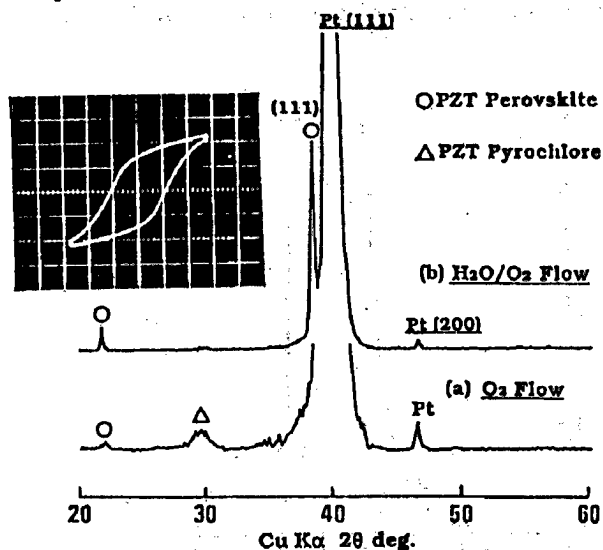

Figure 6. XRD Profiles of PZT (Zr:Ti = 53.47) Thin Films on Substrate (Pt/Ti/SiO$_2$/Si) Fired at 600°C for 2h. Condition of calcination:
  (a) O$_2$ flow; (b) H$_2$O/O$_2$ flow

On SrTiO₃ and MgO substrates it is possible to crystallize a preferred orientation PMN/PT perovskite single-phase film by subjecting it to heating of temperatures higher than 700°C.

On a Pt/Ti/SiO₂/Si substrate it is more difficult to synthesize a single-phase perovskite film. This author's team has found that a preferred orientation PMN/PT perovskite thin film can be synthesized easily on a Pt film by having Mg and Nb alkoxides configured at the B sites of the perovskite and by forming a PZT thin film as an intermediate base film (Figure 8). The dielectric constant of the 0.9 PMN/0.1 PT film at 1 MNz stood at about 1,700. No mutual diffusion was observed between the base PZT film and the PMN/PT layer.

4. Conclusion

The chemical synthesizing method discussed above involving the use of an alkoxide solution produced by controlling reactions between metal alkoxides makes it possible to produce multicomponent oxide thin films having high purity and accurate composition at low temperature. It is challenging to synthesize thin films having intended properties by optimizing the conditions for synthesizing the precursors (molecular building blocks) created by achieving metal-oxygen-metal bonding at the molecular level by controlling reactions in the metal alkoxide and the conditions for crystallizing the precursors, and by considering the substrate structure and crystallographic orientation. At the same time, it is an interesting undertaking when considering the reaction and crystal formation process involved.
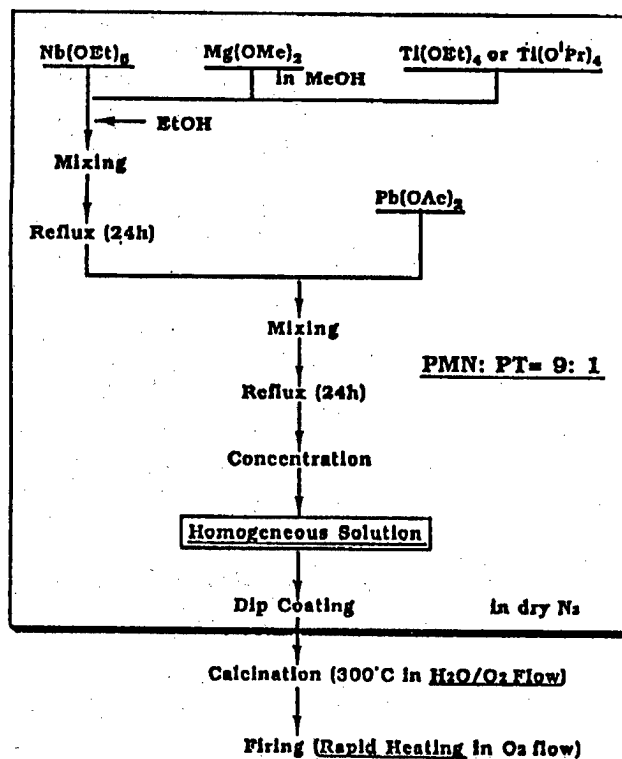
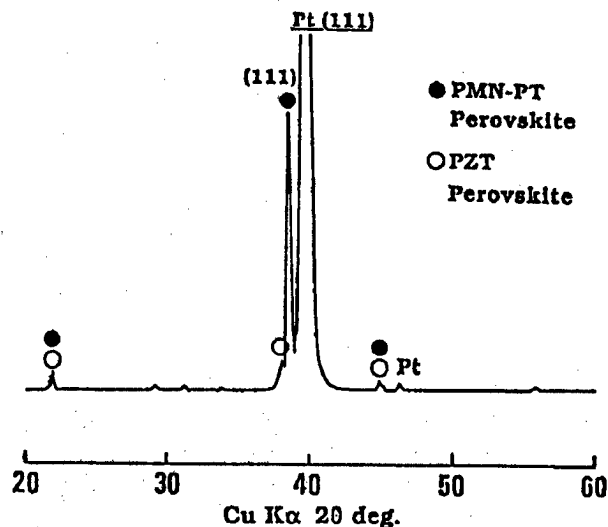Figure 7. Processing Parameters for PMN/PT Films

Figure 8. XRD Profile of 0.9PMN-0.1PT (2%PbO) Film on Substrate (Pt/Ti/SiO₂/Si Fired at 800°C for 1h (on PZT)

15

This thin film synthesizing method can also be used for synthesizing fibers and fine particles and modifying surface conditions in various kinds of other materials.

References

1. Hirano, S. and Kato, K., "Synthesis of $LiNbO_3$ by Hydrolysis of Metal Alkoxides," ADVANCED CERAM. MATER., Vol 2, 1987, pp 142-145.

2. Ibid., "Formation of $LiNbO_3$ Films by Hydrolysis of Metal Alkoxides," J. NON-CRYST. SOLIDS, Vol 100, 1988, pp 538-541.

3. Ibid., "Preparation of Crystalline $LiNbO_3$ Films With Preferred Orientation by Hydrolysis of Metal Alkoxides," ADVANCED CERAM. MATER., Vol 3, 1988, pp 505-506.

4. Ibid., "Preparation of Crystalline $LiNb_xTa_{1-x}O_3$ (0<x<1) Films From Metal Alkoxide Solutions," BULL. CHEM. SOC. JAPAN, Vol 62, 1989, pp 429-434.

5. Ibid., "Processing of Crystalline $LiNbO_3$ Films With Preferred Orientation Through an Organometallic Route," SOLID STATE IONICS, Vol 32/33, 1989, pp 765-770.

6. Ibid., "Processing of Crystalline $Li(Nb,Ta)O_3$ Films With Preferred Orientation Through Metal Alkoxides," MAT. RES. SOC. SYMP. PROC., Vol 155, 1989, pp 181-190.

7. Hirano, S., Kikuta, K., and Kato, K., "Processing of Stoichiometric and Ti Doped $LiNbO_3$ Films With Preferred Orientation From Metal Alkoxides," Ibid., Vol 200, 1990, pp 3-11.

8. Eichorst, D.J., Payne, D.A., Wilson, S.R., and Howard, K.E., "Crystal Structure of $LiNb(OCH_2CH_3)_6$: A Precursor for Lithium Niobate Ceramics," INORG. CHEM., Vol 29, 1990, pp 1458-1459.

9. Budd, K.D., Dey, S.K., and Payne, D.A., "Sol-Gel Processing of $PbTiO_3$, $PbZrO_3$, PZT, and PLZT Thin Films," BR. CERAM. PROC., Vol 36, 1985, pp 107-121.

10. Francis, L.F. and Payne, D.A., "Processing Perovskite Phase Development and Dielectric Properties for Sol-Gel Derived $Pb[(Mg_{1/3}Nb_{2/3})_{0.9}Ti_{0.1}]O_3$ Thin layers, MAT. RES. SOC. SYMP. PROC., Vol 200, 1990, pp 173-178.

11. Hirano, S., Yogo, T., Kikuta, K., Kato, K., Sakamoto, W., and Ogasahara, S., "Sol-Gel Processing and Characterization of Ferroelectric Films," CERAM. TRANS. (in press), 1991.

High-Performance Nanocomposite Ceramics

936C3809C Osaka ATARASHI KINOSEI SERAMIKKUSU in Japanese 2 Mar 92 pp 41-43

[Article by Koichi Niihara, Industrial Science Research Institute, Osaka University]

[Text] 1. **Introduction**

Improvement of the properties of ceramic structural materials has been carried out by controlling the diameter, shape, and porosity in the material powder grains and by controlling grain boundary conditions. However, improvement of properties through these conventional methods has reached its limits and now the introduction of new material-designing techniques is becoming necessary to develop materials of higher performance.

In an effort to introduce new material-designing techniques in the development of high-performance ceramics, this author's team has conducted research by classifying ceramic materials into monolithic materials and composite materials, and by subdividing the composite materials into microcomposite materials, nanocomposite materials, and micro-/nano-hybrid materials. The results have shown that the mechanical properties of ceramic materials can be improved greatly and new functions can be imparted by introducing a nanocompositing technology. These results are described below.

2. **Microcomposite Materials**

Refer to Material 1 (designing of high toughness ceramics) [not reproduced].

3. **Nanocomposite Materials**

Refer to Materials 1 and 2 (sintered nanocomposite compacts) [not reproduced].

4. **Micro-/Nano-Hybrid materials**

Research has revealed that the mechanical properties of ceramic materials can be improved greatly by introducing nanocomposite technology. Despite this improvement, the fracture toughness of these ceramic materials is still lower than their metallic counterparts. However, it has been found that the toughness of ceramic materials can be improved further by reinforcing nanocomposite

17

Table 1. Changes in Strength and Fracture Toughness of Carbon Fiber–Reinforced Sialon/SiC Nanocomposite Fabricated by the Sintering Method

Composite material	Strength (MPa)			Toughness $(MPam^{1/2})$[*1]	
	RT	1,300°C	1,500°C	RT	1,300°C
Long–fiber– reinforced Sialon	314			9.5	
Long–fiber– reinforced Sialon/ SiC nanocomposite	705	1,075	790	25.0	22.0

1) Measured by the V–notch method developed by JFCC.

ceramic materials with long fibers of reinforcing materials, as demonstrated by the data for fiber–reinforced Sialon/SiC nanocomposite materials (Table 1). The strength and toughness of these materials attained under room temperature conditions are superior to that of sintered hard alloy (WC/Co cermet) currently in use widely in industrial applications. As far as this author knows there has been no announcement concerning the successful development of similar materials that maintain their room temperature mechanical properties up to a temperature higher than 1,300°C, with the properties improving further at higher temperatures.

5. Imparting New Functions

Superplasticity can be imparted to Si_3N_4 ceramic material by processing it into a very fine nanocomposite by controlling the sintering conditions to have about 35% of α–Si_3N_4 remain within the sintered composite (Material 2). Another nanocomposite that has nanolevel amorphous SiC in the SiC grain boundaries can be produced by sintering a mixture of SiC powder and polysilastyrene [phonetic] organic compound precursor, that transforms into SiC when fired, at temperatures between 1,600~1,900°C. This nanocomposite has been found to retain most of the room temperature SiC properties at high temperatures, and it displays a high strength of about 450 MPa at 1,500°C. The composite can be processed mechanically with almost the same grindability experienced in machining metallic materials (Material 2). This grindability is believed to relate to the nanosize open pore present in the grain boundaries, and nano–T–level grain diameter.

It has also been found that by promoting nanocompositing, the basic physical characteristics of the composite, such as elastic modulus, thermal–expansion rate, and thermal conductivity, can be controlled.

6. Role of Scattered Nanoparticles

In considering relationships between the microstructure and nanostructure and the mechanical properties in nanocomposite materials, it is believed that the

18

roles which nanoparticles play within these materials differ considerably between oxide systems and nonoxide systems.

The nanocomposite systems, such as Al_2O_3/SiC, Al_2O_3/Si_3N_4, and MgO/SiC, in which matrixes have larger thermal-expansion rates than the scattered phase (and the scattered phase maintains its room temperature hardness up to high temperature) nanoparticles are believed to play the following roles:

1) Finer structure, restraining the growth of abnormal grains, controlling grain shape: reduction strength differences.

2) Deflection of crack propagation direction, generation of microcracks within crystallized grains: improvement of fracture toughness from 1.5~4 times.

3) Generation of subgrain boundaries caused by localized stress occurring within the grains: generation of coarse grains, restraining strength deterioration caused by inhomogeneous material composition, reduction of strength differences, improvement of strength by reducing fracture sources, improvement of high-temperature strength.

4) Induction of fracture within the grains caused by localized stress occurring around the particles scattered within the grains: the deflection of the propagation direction of microcracks attributed to the nanoparticles improves the toughness of nanocomposites. These particles restrain the lagging high-temperature fracture attributed to the presence of impurities in the grain boundaries (improvement of high-temperature strength).

5) Pinning resulting from the movement of dislocation in the hard particles scattering within the material grains under high temperature condition: contributes to improvements in high-temperature hardness, high-temperature strength, fatigue durability, creep resistance, and brittleness/ductility transition temperature (maximum usable temperature under high-load condition).

6) Controlling Young's modulus, thermal expansion rate, and thermal conductivity: improvement of heat-shock resistance as a result of improvements in strength and toughness.

The bar-shaped grains observed in conducting liquid-phase sintering of Si_3N_4 is believed to be produced as a result of dissolving $\alpha-Si_3N_4$ into the melted phase present in the grain boundaries under a high temperature. The melted phase is generated as a result of addition of sintering-promotion agents. The grains are synthesized when $\alpha-Si_3N_4$ reprecipitates as $\beta-Si_3N_4$. So, by using Si-C-N composite powder as a starting material, the nanocompositing of the powder is believed to be realized due to the SiC grains deriving from Si-C-N powder under high temperature scattering to work as growth nuclei when the bar-shaped $\beta-Si_3N_4$ homogeneously precipitates from the grain boundary liquid phase. The SiC grains are taken into Si_3N_4 grains in this process. Increasing the number of SiC grains as the growth-promoting nuclei restrains the growth of the bar-shaped Si_3N_4 grains, causing finer structure in nanocomposites. From these observations, the scattered nanograins in this material system are believed to play the following roles:

19

1) The scattered SiC grains promote the precipitation of bar–shaped β–Si$_3$N$_4$ from the melted phase, and this contributes to an improvement in fracture toughness and strength.

2) The SiC grains scattered in the grain boundaries control the boundary structure, contributing to an improved high–temperature strength in nanocomposites.

3) An increase in the number of these SiC grains causes a decrease of Si$_3$N$_4$ grain diameter, and this, under proper conditions, makes it possible to synthesize nano–nanocomposites having superplasticity.

7. Future of Ceramic Structural Materials

Research on ceramic nanocomposites has just begun and there are many problems that must be solved. These problems include whether the calculated values of the residual stress present inside and outside of these scattered nanoparticles are correct; when and how the subgrain boundary is created; toughening, by the combined effects of crack propagation direction deflection by nanoparticles and the presence of microcracks; and what roles the nanoparticles having reverse–thermal–expansion rates compared to the systems discussed above, play. However, in the ceramic systems whose data are given in Table 1, nanocompositing greatly improved the ceramic material's mechanical characteristics. Future ceramic structural materials are expected to be used in monolithic, microcomposite, or nanocomposite form depending on application requirements. Considering the performance of the microcomposite and nanocomposite materials introduced in this report, it is expected that ceramic materials having excellent toughness even at high temperature can be developed by combining microcomposite and nanocomposite materials. It is believed that long–fiber–reinforced nanocomposite materials will play a central role in the development of these ceramic materials.

It appears that nanocompositing technology can be used to impart new functions to ceramic materials. This author concludes this report with the hope that research on nanocomposite ceramic materials will be expanded and increased.

Nonlinear Optical Glass Material

[Article by Setsuro Ito, New Glass Development Institute, Asahi Glass Co., Ltd.]

[Text] 1. Introduction

The increase in communications volume in the next century will promote the introduction of optical communications facilities to handle and process a huge amount of information at higher speed. This will call for the use of various light-transmission controlling materials. Among these materials, nonlinear optical materials in which the transmissivity and refractive index change in accordance with the strength of incident light will be indispensable to create light switches, optical memory, and conjugate-phase elements. Currently, active research and development efforts are paying much attention to glass as a nonlinear optical material because it is superior to other candidate materials in transparency, durability against strong laser-light exposure, and moldability.

This paper will report on the results of this author's research on nonlinear optical glass by focusing on the synthesizing method of fine-particle scattered glass and its characteristics.

2. Nonlinear Optical Characteristics

In general, the polarization, P, caused by optical electric field E is expressed as[1]

$$P = \chi^{(1)} E + \chi^{(2)} E^2 + \chi^{(3)} E^3 + \cdots \qquad (1)$$

where $\chi^{(n)}$ is called nonlinear susceptibility . The nonlinear characteristics become more pronounced when the susceptibility increases. Commonly, in the materials that have an inversion symmetry, such as glass, the $\chi^{(2)}$ term does not appear, making $\chi^{(3)}$ dictating the nonlinear characteristics. In $\chi^{(3)}$, nonlinear characteristics, the refractive index n and absorption coefficient α change depending on the strength of the light, and n and α are expressed as:

$$n = n_0 + \Delta n = n_0 + (\text{Re}\chi^{(3)}/2\epsilon_0 n_0) \; E^2 \qquad (2)$$

$$\alpha = \alpha_0 + \Delta\alpha = \alpha_0 + (\omega \text{Im}\chi^{(3)}/\epsilon_0 n_0 C) \; E^2 \qquad (3)$$

where $\text{Re}\chi^{(3)}$ and $\text{Im}\chi^{(3)}$ represent the real part and imaginary part of $\chi^{(3)}$, n_0 and α_0 denote the linear refractive index and absorption coefficients, and ϵ_0, C, ω, the dielectric constant, light speed, and frequency, respectively.

Generally, the value of $\chi^{(3)}$ is very small, and consequently that of n_2 and α_2 are also very small, making their effects almost negligible in ordinary light in which the optical electric field strength is weak. However, in recent years, high-powered lasers and new materials having higher values of $\chi^{(3)}$ have begun to appear and the effects of the refractive index and the absorption coefficients are no longer ignored. Taking advantage of this nonlinearity, research is now being conducted to develop various types of new optical elements.
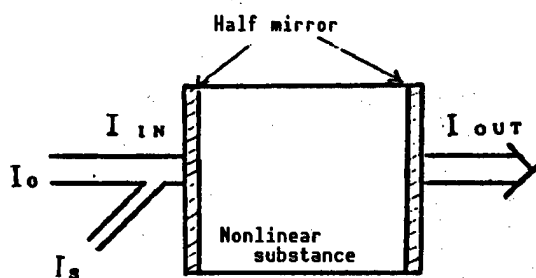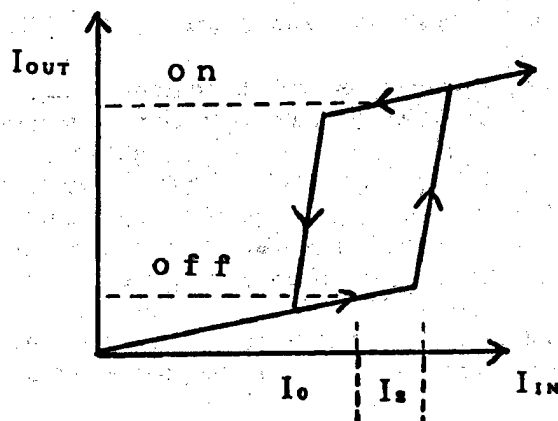

Figure 1. Fabry–Perot Resonator

Figure 2. Optical Switching Characteristics

An optical switch shown in Figure 1 is an example of this. In the switch, feeding a signal light pulse, Is, to a Fabry–Perot resonator having a bias light ion (off state) causes a change in the refractive index of the switching material, causing a change in the strength of the outgoing light (on state), as indicated in Figure 2.[2] This switching device can also be used as an optical memory because the on state can be maintained even after the Is is cut off by a light stabilizing effect.[2] In order to create an optical switch having the above capability, the phase difference caused by a change, Δn, in the refractive index must be made larger than half the wavelength, and consequently the following equation can be derived:

$$\chi^{(3)} \geq n_0^2 \cdot \lambda \times 10^{-5}/I \cdot L \qquad (4)$$

where I denotes light strength in MW/cm^2, λ the wavelength in μm, and L the interaction length in μm.[3]

To promote the application of such a light switch it must be capable of performing information processing at a superhigh speed. This requires the operation speed to be around 1 picosecond or faster by satisfying the following equation[3]:

$$n \cdot L/C \leq 1 \; ps \qquad (5)$$

22

Provided n - 1.5, the value of L must be lower than 200 μm from Equation (5).
And when I - 10 MW/cm^2 and η - 1 μm, the value of $\chi^{(3)}$ must be higher than 10^{-8}
esu from Equation (7). To make the incident light exit the switching device
with almost no power loss, the condition expressed by the following equation
must be met:

$$\alpha \cdot L < 1 \tag{6}$$

In addition to optical switches, nonlinear optical glass could be used to
develop other optical communications and peripheral devices, including optical
exchangers, optical connectors for interconnection between electrical devices,
optical memory, and conjugate phase mirrors. In all these applications, the
value of $\chi^{(3)}$ must be as large as possible.

3. Kinds of Nonlinear Optical Glass

3.1 Homogeneous Nonlinear Optical Glass

High-refractive index homogeneous glass displays more pronounced nonlinear
optical characteristics than conventional glass because of changes in the
refractive index caused by electric polarization occurring within the glass.
In this type of glass, light having the wavelengths in the nonresonance range
is used, making it possible to confirm the absorption coefficients at a low
level and achieve fast nonlinear response speed. However, this type of glass
has lower $\chi^{(3)}$ values, as given in Table 1. This makes it necessary to process
the glass into a fiber for use in switching operations by setting the
interaction length at about 1 m. For this kind of application, As-S-Se-system
chalcogenide glass is regarded as a promising candidate.

Table 1. Nonlinear Susceptibility in Homogeneous Glass

	$\chi^{(3)}$ (esu)
SiO_2	3×10^{-14}
SF-6	5×10^{-14}
$Li_2O-TiO_2-TeO_2$	10^{-12}
$Na_2O-SiO_2-TiO_2-Nb_2O_5$	10^{-13}
Ge-As-S	5×10^{-12}
As-S-Se	10^{-11}

3.2 Scattered Particle Nonlinear Optical Glass

A scattered fine-particle-containing glass with particle diameter ranging from
10-100 Å is made to display high $\chi^{(3)}$ nonlinear optical characteristics by
confining electrons, holes, or excitons within these particles. Such a glass
is expected to realize a superhigh response speed (faster than 10^{-12} sec), thus
making the glass a promising material for use in optical switches and optical
memory devices. By using a sharply-cut glass filter having scattered superfine
semiconductor particles of CdSxSe1-x, high values of $\chi^{(3)}$ have been attained.[4]
Research on this scattered-particle glass has been stepped up since finding an

23

optical switching characteristic in glass, as shown in Figure 3.[5] As candidate hosts for accommodating these superfine particles, plastics, and the media in the form of solution and crystal can also be used, in addition to glass. However, glass is believed to be the most suitable for the following reasons:
1) ease of controlling the scattered particles; 2) higher optical quality; and 3) ease of creating light transmission channels and process into a fiber form.

Table 2 gives the nonlinear susceptibility $\chi^{(3)}$ in a number of kinds of glass containing different types of superfine particles. As seen in the table, there are already some glasses having susceptibility levels higher than 10^{-6} esu.
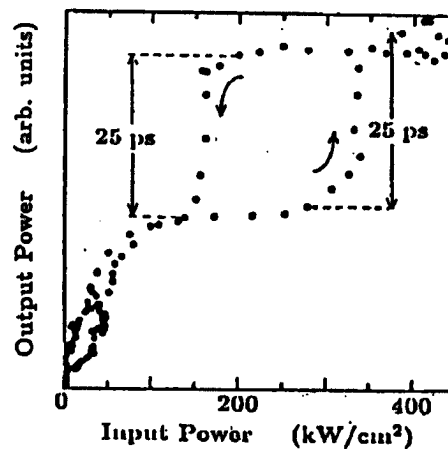

Figure 3. Input-Output Characteristics of Fabry-Perot Resonator

Table 2. Nonlinear Susceptibility in Fine Particle-Scattered Glass

		$\chi^{(3)}$ (esu)
MnO	melt-precipitation method	2×10^{-9}
CdS_xSe_{1-x}	"	10^{-8}
CdSe	"	10^{-6}
CuCl	"	10^{-6}
Au	"	10^{-11}
Au	sputtering method	10^{-7}

These superfine-particle-scattered glasses are produced by the melt-precipitation method, porous impregnation method, sol-gel method, or gas-phase method. Nonlinear optical characteristics of glass created by these methods differ greatly depending on the kinds of particles used, the scattering conditions, and the particles' density and diameter. This makes it important to develop an effective method to control these particle parameters.

This author's group is engaged in the development of a glass containing superfine particles of CuX (X = Cl,Br) semiconductor crystal. This semiconductor crystal is believed to be capable of realizing high nonlinear optical effects by confining the quantum caused by the small-Bohr radius of the excitons. The glass synthesizing method, its microstructure, and the optical characteristics centering on the $\chi^{(3)}$ nonlinear characteristics are described below.

4. CuX Particle Scattered Nonlinear Optical Glass

4.1 Synthesizing of the Glass and Its Structure

To create base glass having a precipitation of CuX fine particles, a photo-chromic glass system (Na_2O-B_2O_3-SiO_2 system) containing fine AgCl particles, the same type of compound as CuX, was used. The different types of glass were synthesized by mixing batches of glass material and other material components (content of CuCl - 1 mol against 100 mol of the glass materials) by introducing silicic anhydride, boric acid, sodium carbonate, and cuprous chloride and by heating 100 cc of the mixture within a platinum crucible in the air at temperatures ranging from 1,300~1,400°C for two hours. The melted crucible contents were poured onto a steel plate, pressed between two steel plates, and cooled. After retaining these glass specimens for one hour at different annealing temperatures they were cooled in an electric furnace. Then, in order to have fine CuCl particles precipitate within these specimens, they were subjected to heat treatments by changing temperature between the glass crystal transition points and the softening points. The precipitation of fine CuCl particles within these specimens was confirmed by the measurement of the adsorption spectrum characteristics. When CuCl precipitates, an absorption spectrum spike appears near the wavelength of 380 nm (Figure 4). In the glass composed of the above three material components, it has been found that CuCl precipitates more easily in a composition in which the content of Na_2O is low and that of B_2O_3 high.

Figure 4. CuCl Precipitated Glass Composition

On the other hand, in the CuBr system, the area in which fine particles precipitate was found to be a little larger than that for the CuCl system; however, almost the same measurement results as those shown in Figure 4 have been obtained.

In order to understand the precipitation mechanisms of CuX, the absorption spectrum in the preheat treatment glass specimens over a range from near-infrared to visible radiation wavelengths was taken by focusing on the behaviors of Cu ion within these glasses. Figure 5 shows the absorption spectra for those CuCl-system specimens, numbering from 1~4 in Figure 4, in the wavelength range between 500~900 nm. Each specimen displays a broad absorption peak at a wavelength near 780 nm caused by Cu^{2+} ion absorption
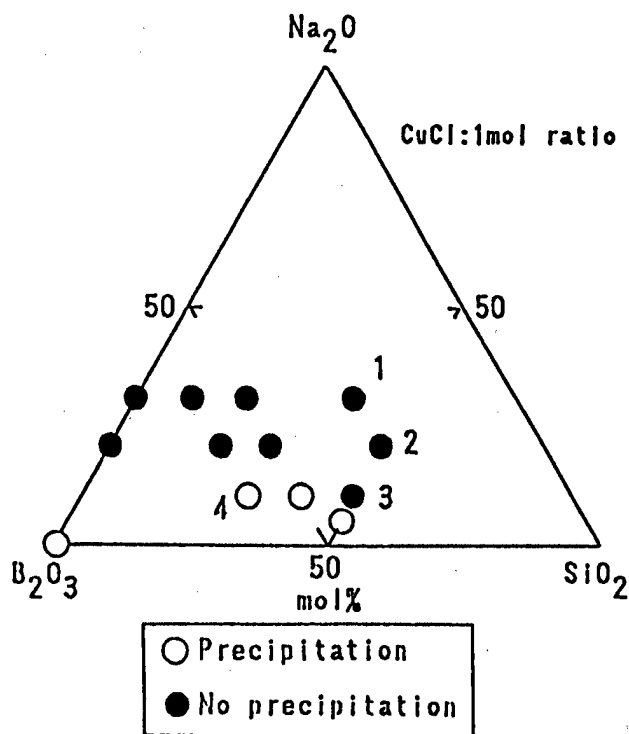
25

within these glasses. Within glass, Cu usually exists in the form of Cu^{2+} and Cu^+, and CuCl precipitates from a glass composition in which the content of Cu^{2+} is low and that of Cu^+ high.

It is believed that oxidation/deoxidation of ions within glass changes depending on the basicity of the glass. This author has calculated the optical basicity of these glasses using the equation proposed by Duffy, et al.[6] Figure 6 gives the results of calculations of the optical basicities (Λ) in the above three component glass specimens. The figure indicates that Λ values decrease in the order of Nos. 1, 2, 3, and 4. From these results and Figure 5, it has been found that the lower the basicity, the lower the absorption of Cu^{2+} ions. This ensures the stable presence of Cu^+ ions within the glass.
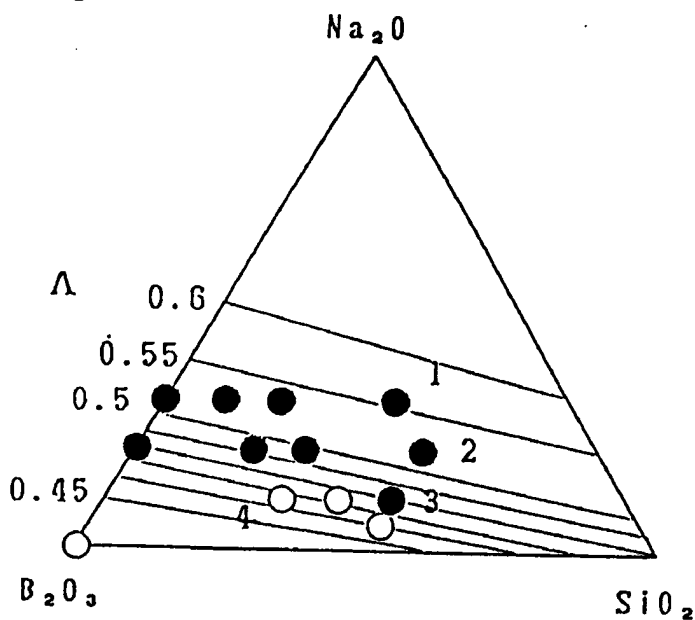

Figure 5. Absorption Spectra in CuCl-System Glass

Figure 6. Basicity in Glass

In an effort to improve the stable presence, a fifth specimen (No. 4 composition + $7.5Al_2O_3 \cdot 0.55SnO$) was created. The SnO was added as a thermal reduction agent and the Al_2O_3 was introduced to improve the stability of the glass. The absorption spectrum of the No. 5 specimen for wavelengths between 500~900 nm is given in Figure 5. With the addition of SnO, the absorption near 780 nm disappeared almost completely, indicating improved Cu^+ stability within the glass. Similar results were obtained with the CuBr system.

4.2 Precipitation of Fine Particles

By creating $10Na_2O-52.5B_2O_3-7.5Al_2O_3-30SiO_2-0.75CuCl-0.325SnO$ (mol ratio) composition glass specimens and treating them for 30 minutes under different temperatures, the microstructures of the precipitated fine CuCl particles were studied by transmission electron microscope (TEM). Figure 7 [not reproduced] shows the TEM image of one of these specimens that was treated at 435°C for 30 minutes.
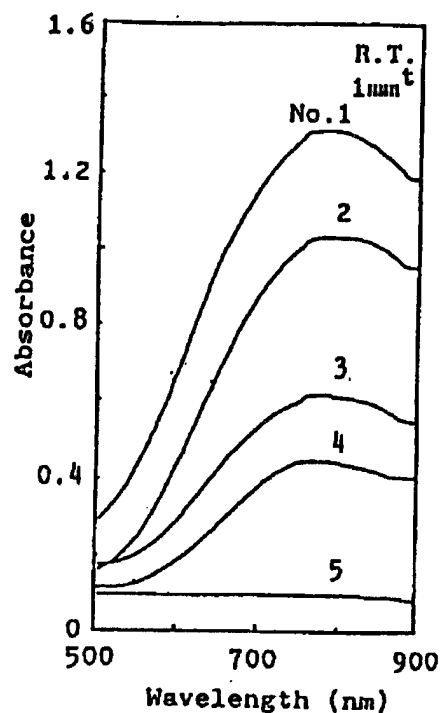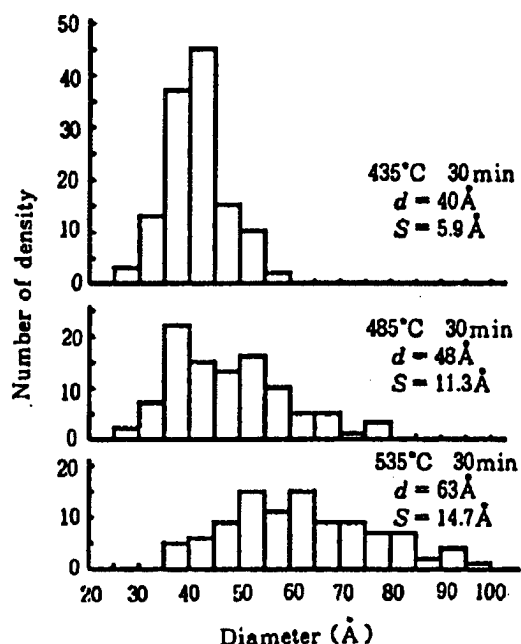
26

Figure 8. Relationship Between Particle Diameter Distribution and Heat-Treatment Temperature in Fine CuCl Particles

WAVELENGTH (nm)

Figure 9. Absorption Spectra in Fine-Particle-Scattered Glass

It can be seen that circular particles ranging in diameter from 30~60 Å randomly scatter over the surface of the specimen. From these TEM images, the particle diameters and the diameter distribution pattern of the precipitated CuCl particles have been studied (Figure 8). Results indicate that the average diameter of these particles increased as heat-treatment temperature increased, and the deviation of particle diameter narrowed when the heat- treatment temperature decreased.

Figure 9 gives the absorption spectra at 77 K for the CuCl-system and CuBr-system specimens that were prepared by changing heat-treatment temperatures. As seen in the figure, absorption peaks appear at two places in those specimens subjected to heat treatment. These peaks were caused by absorption by the excitons (Z_{12}, Z_3), as they shifted toward the low-energy side (longer wavelength side) and the peaks became higher as heat-treatment temperature increased. Almost the same results were obtained by lengthening the treatment time while keeping the treatment temperature the same. In the figure, the
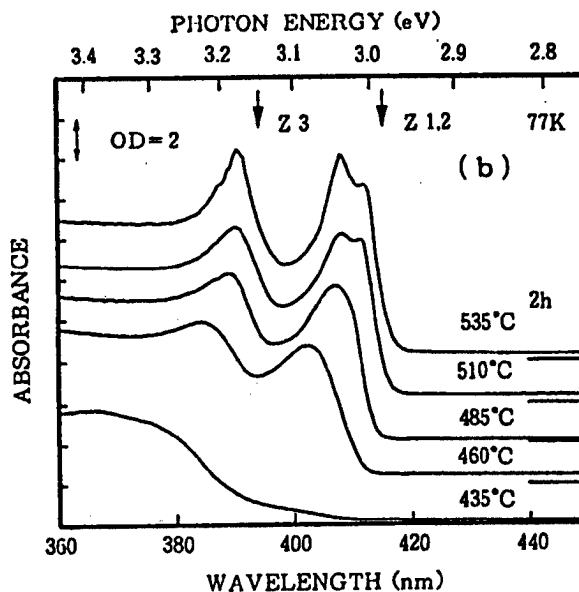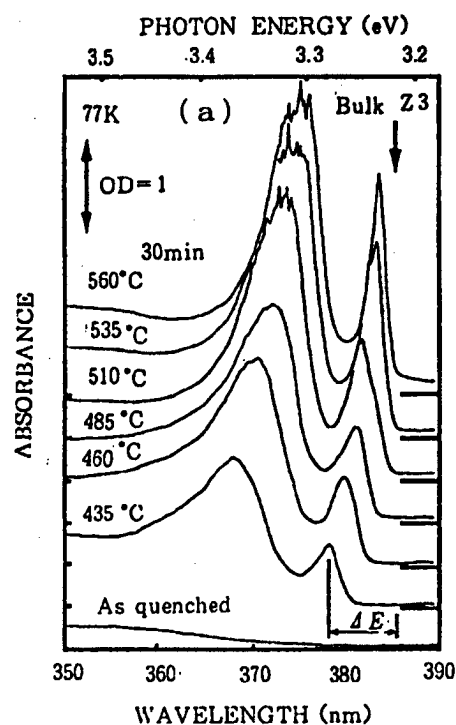
arrows indicate the absorption points of Z_3 exciton in the bulk crystal. The degree of shifting of the absorption points of Z_3 exciton from that of the bulk crystal ranged from about 10~40 meV in either of the systems, and the degree of shifting diminished as the heat-treatment temperature increased.

The electrons and holes within the fine semiconductor particles scattering within the glass are confined within the three-dimensional space defined by the deep potential produced by the matrix glass. The shifting energy, ΔE, under this condition in which the excitons are confined within the fine particles through the quantum confinement effects is expressed by the following equation[1]:

$$\Delta E = (2M)^{-1} h^2 \pi^2 a^{-2} \qquad (7)$$

where M denotes the translational mass of electrons and holes, h the Planck's constant, and a represents the radius of the fine particles. Figure 10 shows the relationships between the ΔE and the radius of the particles, with the data
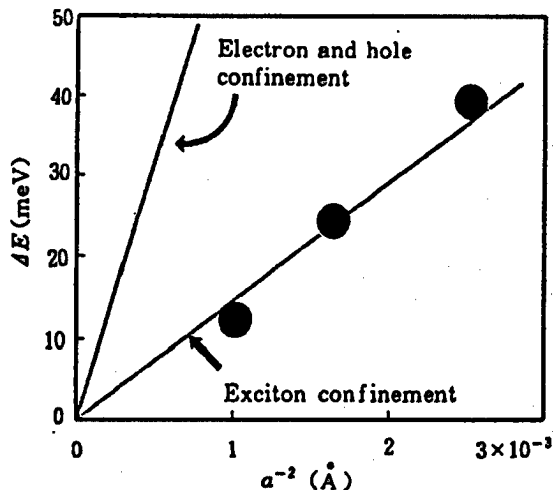
Figure 10. Relationship Between Fine Particle Radius and Exciton Energy Shift
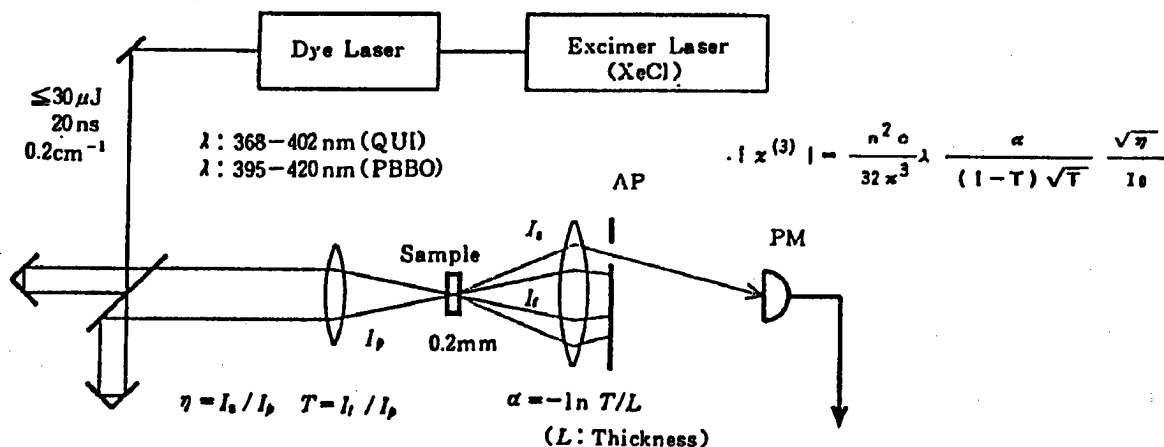
Figure 11. Schematic Representation of Forward-Incident Degeneracy Four-Light Wave Mixing Method

obtained through TEM observation of the average radius and the absorption spectrum measurement. In the figure, the relationships represented by the above equation when M takes a value of 2.83 m_0 is shown by the straight line. It has been found that the value of ΔE changes in proportion to the changes in a^{-2} value and the measured values almost coincide to the calculated values. So it has been found that in using the above equation it is possible to know the diameter of the fine CuX particles scattered within glass by measuring the absorption energy of Z_3 exciton. Based on this finding, this author calculated the diameter of the particles precipitated within the specimens treated at different temperatures by measuring the absorption energy of the Z_3 exciton.

28

The results found that in the high-temperature side, the particle grew larger in the CuBr system than in the CuCl system. It was also found that fine particles with diameters ranging from 30–300 Å can be grown by selecting appropriate heat-treatment temperature and the appropriate length of treatment time.

4.3 Nonlinear Optical Characteristics

The nonlinear susceptibility ($\chi(3)$) of a number of types of glass was measured by the forward incident-type degeneracy-four light wave mixing method (Figure 11). Glasses having $10Na_2O-52.5B_2O_3-7.5Al_2O_3-30SiO_2-0.5CuX-0.25SnO$ (mol ratio) composition have been created as specimens for heat-treating measurements at different conditions. These specimens contained CuX particles having different diameters.

Figure 12 shows the relationship between the diameters of these fine particles and $\chi^{(3)}$ absorption peak wavelength values of the Z_3 exciton in each of these specimens when incident light strength is 10 kw/cm². The figure shows that $\chi^{(3)}$ takes the maximum values when particles have appropriate diameters. Figure 13 gives the relationship between the $\chi^{(3)}$ and the wavelength. The figure indicates that in either system $\chi^{(3)}$ takes the largest values at the wavelengths where the absorption maximizes. As can be seen from the figure, it is possible to obtain values higher than 10^{-6} esu.

Figure 12. Relationship Between $\chi^{(3)}$ and the Fine Particle Diameter

5. Conclusion

This author has studied the nonlinear optical characteristics of glass containing CuX particles by creating CuX particle-scattered glass specimens by the melt-precipitation method. CuX particle-scattered glass theoretically
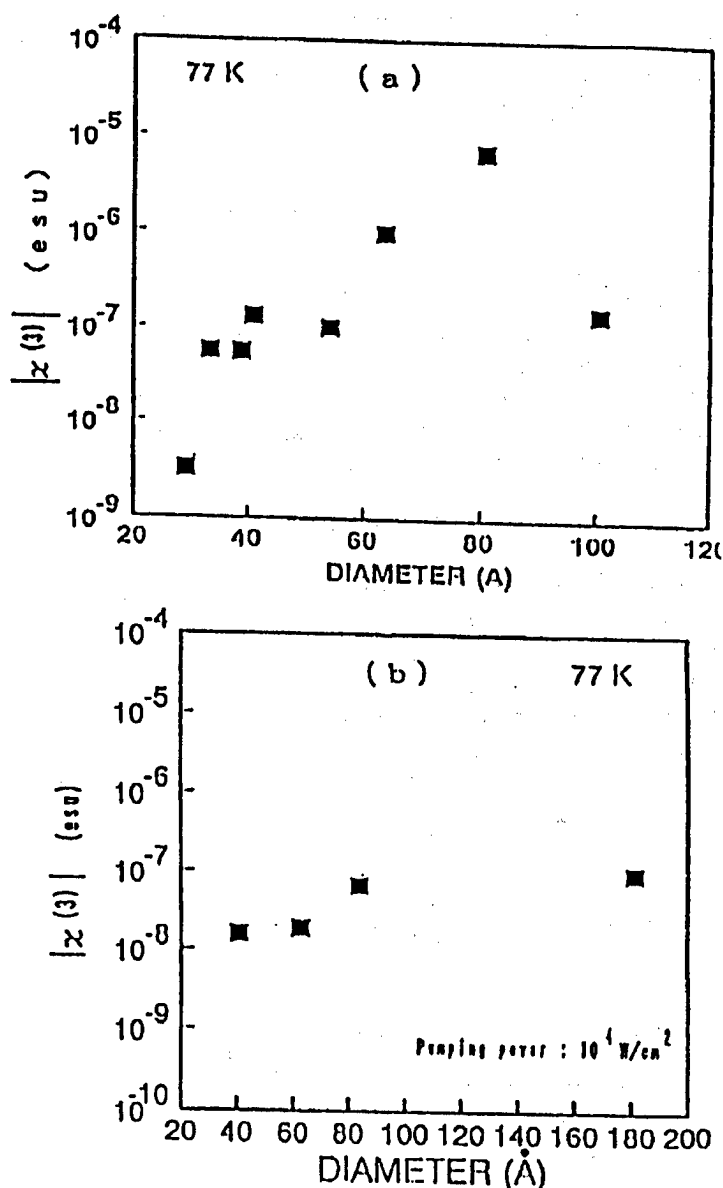
29

makes it possible to enhance the nonlinear characteristics by making the particle finer. The study found that in borosilicate—system glass it is possible to precipitate fine CuX semiconductor particles having diameters ranging between 30~300 Å by controlling heat—treatment conditions. It was also found that the nonlinear susceptibility of the glass changes greatly depending on the scattered particle diameter and the wavelength of light. Under experimental conditions it was found that susceptibility reaches values higher than 10^{-6} esu.

Experiments have achieved high $\chi^{(3)}$ values in a few types of superfine particle scattered glass, including the one containing CuX systems. Continued progress in this field of research will make it possible to develop glass—based optical controlling devices in the near future. However, there are still many problems that must be solved before realizing this. They include the necessity to make response time faster, smaller than 1 picosecond, and lowering the absorption coefficients below 100 cm^{-1} while maintaining high $\chi^{(3)}$ values. The techniques for analyzing and evaluating the nonlinear characteristics and measuring the response time must also be developed.

Figure 13. Relationship Between $\chi^{(3)}$ and the Wavelength

To promote progress in this research, it is essential to push comprehensive research encompassing material development, device development technology, and analytical evaluation technology.

6. Acknowledgements

What has been described in this paper is based on results that have been obtained by conducting research as part of the next—generation basic industrial technology development project, with the research entrusted to this author's institute by the New Energy Development Organization via Kobunshi Sozai Center. Evaluation of nonlinear photoelectron characteristics was conducted in cooperation with a research team led by Professor Arao Nakamura of Nagoya University's Department of Engineering.

30

References

1. Nakamura, A., OPTICAL ENGINEERING, Vol 19 No 1, 1990, p 10.

2. Abraham, E., et al., SCIENCE, No 4, 1983, p 48.

3. Shimizu, A., "Quantum Effects and Optical Switching," In "Ultra High-Speed Optical Switching Technology," edited by T. Kamiya, et al., Baifukan, 1992.

4. Jain, R.K., et al., J. OPT. SOC. AM., Vol 73, 1983, p 647.

5. Yumoto, J., et al., OPT. LETT., Vol 12, 1987, p 832.

6. Duffy, et al., J. NONCRYSTALLINE SOLID., Vol 21, 1976, p 373.

Nonlinear Optical Material Using Dielectric Crystal

[Article by Takatomo Sasaki, Osaka University Department of Engineering]

[Text] 1. Introduction

In recent years active research has been conducted to obtain green, blue, and ultraviolet light through light-wavelength conversion based on the nonlinear optical effects in crystallized dielectric substances. Needs for visible as well as ultraviolet light sources have been mounting for use in ultraviolet beam lithography, medical applications, machining, and nuclear fusion. The fine tunability of the wavelength is required for the lights used in the fields of photochemical reactions, and isotope separation using lasers. For application to optical information processing, computer displays, and optical measurement, the development of compact, light, and long-service-life light sources capable of providing green, blue, and ultraviolet light is needed. Current efforts by researchers are aimed at developing solid-state lasers to replace conventional bulky, comparatively short-service-life, not easily-maintainable gas-discharge lasers and liquid lasers. Researchers are trying to obtain lights having wavelengths up to that of ultraviolet rays through the wavelength conversion using nonlinear optical materials. Toward these ends, researchers have made efforts to develop organic/inorganic nonlinear optical crystals for their application to the development of optical devices.

Polarization caused when a substance was irradiated with a light having an electric field strength E is expressed by the following equation:

$$P = \chi^{(1)} E + \chi^{(2)} E \cdot E + \chi^{(3)} E \cdot E \cdot E + \cdots$$

Usually, the coefficients in the orders lower than $\chi^{(2)}$ are ignored because their values are smaller than that of $\chi^{(1)}$. In the case of a laser light having a powerful electric field strength E, the contributions by the higher orders of these χ terms increase, making a dielectric substance exhibit nonlinear optical effects. The value of $\chi^{(2)}$ assumes zero when a substance has a symmetrical crystal structure. However, χ does not take zero value. The effects produced by the terms higher than $\chi^{(2)}$ include the second higher harmonics generation (SHG), sum frequencies and difference frequencies, and wavelength conversion by parametric oscillation. In recent years, extensive

research has been conducted on the effects of $\chi^{(3)}$ for application to high-speed optical switching, and the photo-refractive effects for use in optical information recording. This paper will describe the materials in which the greatest progress has been made in the efforts to apply them to the development of wavelength-conversion devices. Developments in wavelength-conversion technology will also be introduced.

The dielectric crystals to fabricate wavelength-conversion devices are required to:

(1) have high nonlinear optical coefficient d $(\chi^{(2)}/2)$;
(2) have high angular as well as temperature tolerances for making the phase matching easy;
(3) have wide transmission range in operating wavelength;
(4) have high laser-damage-resistance capability;
(5) be easily grown into optically excellent large crystal;
(6) have high chemical stability, particularly good antihumidity capability;
(7) be mechanically strong and easy to process; and
(8) be inexpensive in material costs.

At present, no crystal is available that satisfies all these requirements. Under the circumstances, in practical applications those types currently available can be used by choosing the type that best meets the requirements of a specific application.

2. Inorganic Nonlinear Optical Materials

The nonlinear properties in inorganic nonlinear optical materials are caused by the constrained electrons within the molecules of these materials. Those that contain P-O, I-O, Nb-O intermolecular bonding structures manifest strong nonlinear effects. Those materials having such bonding structures are KDP(KH_2PO_4) family, $LiIO_3$, $LiNbO_3$, $KNbO_3$, and $Ba_2NaNb_5O_{15}$ (BNN).

Chalcopyrites such as AgGaS have high Nicaloceram optical coefficients. However, their use is currently confined to infrared and near-infrared applications because of their narrowband gap. In China, excellent inorganic crystals for ultraviolet-ray generation, such as beta barium borate (BBO) and lithium borate (LBO) have been developed recently.

2.1 Materials for High Power Lasers

Crystals for use in wavelength conversion of high power lasers are required to have high laser-damage-resistance capability and have the properties that make it possible to grow large optically excellent crystal. Representative nonlinear optical crystal materials for use in high power laser applications are KDP, KTP, BBO, and LBO.

For use in high power output, such as high repetitive action frequency lasers, nonlinear optical crystals are required to have high heat-withstanding capability and high conversion efficiency. For the conversion of a light

33

having a wavelength of 1 μm, KTP crystal is the most suitable, and for the generation of ultraviolet rays, BBO and LBO are preferred. Crystal for these applications must have high heat-shock withstanding capability and be nonwater-soluble.

KDP crystal has been used in practical applications for a long time because the material can be grown into a large crystal, is transparent up to a wavelength of 200 nm, and can withstand laser damage. Currently, it is possible to grow a KDP crystal having a diameter of 45 cm and a height reaching about 1 m for use in the generation of the third harmonics (0.35 μm) for nuclear fusion experiments.[3] Figure 1 [not reproduced] shows large KDP crystals created by this author's group. They are water-soluble, thus making it difficult to grind them and apply a nonreflective (AR) coating. However, recently better grinding methods and an AR coating technology[4] have been developed which alleviate this problem.

KTP crystal has many advantages that make it useful for practical applications. The advantages include a high conversion efficiency (nonlinear optical coefficient d being higher than 10 times that of KDP), high temperature and incident laser light angular tolerances (25°C·cm, ~50 mrad·cm), nonwater-solubility, and high material hardness and strength. The defect of the crystal is its inability to attain phase matching at wavelengths shorter than 1 μm, although it has a transmission wavelength range extending up to 0.35 μm. KTP crystal can be grown by the hydrothermal method or flux method. Figure 2 [not reproduced] shows a KTP crystal grown by this author's group in about 40 days. The crystal, measuring 32 x 42 x 87 mm^3 (a x b x c axes), was grown by using K6Flux and by cooling the temperature from 960°C. Considering that the flux method makes it possible to grow a crystal comparatively easily, it could be possible to grow a still larger crystal. In KTP crystal, the refractive index changes when it grows. Because of this, it has been found recently that the phase-matching angle for generating the second harmonics changes depending on the locations on the crystal (Figure 3).[5] This must be taken into account in using the crystal in practical applications. KTP is also useful as a material for fabricating a low-power-laser wavelength converter and parametric oscillators for generating lights with wavelengths ranging between 1.5~2 μm.
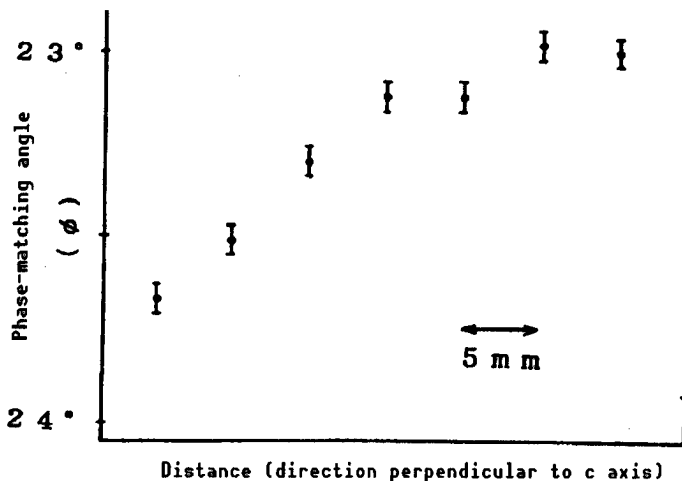
Figure 3. Change of the Phase Matching Angle Depending on the Locations on a KTP Crystal

BBO (β-BaB$_2$O$_4$) crystal elicits interest because it can generate ultraviolet rays having wavelengths shorter than 0.2 μm at high efficiency. It has a nonlinear optical coefficient value 4.4 times that of KDP type II and a large temperature tolerance of 23°C·cm. The crystal has a high laser-damage withstanding threshold

value, but it is not completely water—insoluble. The crystal has an incident laser light angular tolerance about half that of KDP, and the conversion efficiency deteriorates when used with laser lights having wide divergent angles and lasers involving high repetitive action frequency. BBO crystal was first grown successfully at a Fujian research center in China by the flux method. Since then, similar BBO crystals have been grown successfully at Cornell University and Stanford University in the United States. Recently, NEC Corp. has attracted attention by successfully growing high quality BBO crystals by the melt method.[6] High hopes are being placed on the melt method because it prevents mingling of flux in the crystal and is suitable for volume production. Research is being conducted to use BBO crystal to generate super—short wavelength (VUV) light shorter than 200 nm,[7] and to generate a laser light having a wide wavelength range using optical parametric oscillators (OPO).[8]

LBO ($LiB3O_5$) crystal was also grown for the first time at the Chinese Research Center,[9] and with as a wide range of transmission factors extending in wave—length from 160 nm to 2.6 μm. The crystal has a comparatively wide incident laser light angular tolerance close to that of KTP. However, its nonlinear optical coefficient is 2.5 times that of KDP, and this is slightly lower than that of BBO. It has a transmission wavelength range extending up to 160 nm, however, phase matching cannot be made up to 555 nm in fundamental wave. However, the crystal can be used in generating Nd:YAG 3ω optical sum frequency (1.06 μm + 0.35 μm = 0.355 μm), and a conversion efficiency of 70 percent has been reportedly realized using a 12.6 mm long LBO crystal. LBO crystals are grown by the top—seed flux method. It is reported that LBO crystals have high laser—damage threshold values thanks to their crystal structure that prevents mingling of impurities into the crystal during the growth process. LBO has been developed recently and its application fields have yet to be developed The d value of the crystal is not very high. However, the crystal could be used for generating CW ultraviolet rays by fabricating internal resonator—type devices because the crystal has low operational loss.

2.2 Materials for Low-Power Lasers

Needs for inexpensive, long—service—life light sources for generating laser beams in the green—blue wavelength range are mounting for use in high—density optical memory disk application and other fields. Lab—level laser oscillations have already been achieved using the II—VI group semiconductor materials. However, at least five more years would be required before practically usable semiconductor lasers become available. On the other hand, efforts to develop wavelength conversion technology are beginning to produce very good results by conducting experiments combining conventional inorganic nonlinear optical materials, such as $LiNbO_3$ (LN), $LiTaO_3$ (LT), and KTP, with a pseudo—phase matching technology. At present, it is not clear which will become usable first on a commercial basis—the II—VI group semiconductor lasers or the technology for the wavelength conversion of near—infrared lasers.

$LiNbO_3$ Crystals and $LiTaO_3$ Crystals: Among the nonlinear optical coefficients in $LiNbO_3$, the diagonal element d_{33} has a large value of 40 pm/V. The d_{33} element is not suitable for use in the angular matching, but can be used in

Cherenkov radiation mode as well as pseudo-phase matching mode wavelength conversions. Until recently, active research has been conducted on the wavelength conversion using the Cherenkov radiation mode involving the use of $LiNbO_3$ waveguide. Today, emphasis is shifting to the development of the pseudo-phase matching method by making use of the domain reversal effect. Experiments have been conducted by using $LiNbO_3$ substrates, $LiTaO_3$ substrates, and $LiNbO_3$ optical fibers.[10] Figure 4 shows the schematic diagram of a device for generating double harmonics by the pseudo-phase matching method involving the use of the waveguide.

Figure 4. $LiNbO_3$ Waveguide Device for Double Harmonics Generation Incorporating Pseudo-Phase Matching Technique by Making Use of the Domain Inversion Effect

The most advanced result reported to date concerns the generation of a blue light with an output power higher than 10 mW using Ti:sapphire laser light source and a device equipped with an $LiTaO_3$ waveguide having excellent laser-damage-withstanding capability.[11] Table 1 gives the methods for causing the domain inversion in $LiNbO_3$ and $LiTaO_3$ that have been developed to date.[12] Among these methods, the one using an electron beam draws particular attention as a method that could be used to cause a bulk mode conversion.[13]

Figure 5. Block Diagram of Structure of a Device for Generating Double Harmonics of a Semiconductor Laser
    The device incorporates a $KNbO_3$ monolithic ring-type external resonator.

$KNbO_3$ crystal attracts attention because it has high d_{32} value suitable for use in bulk-type wavelength inversion at high efficiency. Figure 5 is a schematic diagram of a blue-light generation system employing an external resonator setup.[14] The system uses a 7 mm $KNbO_3$ ring-type monolithic resonator to effect wavelength conversion. In this method, it is important to match the wavelength between the laser light and the external resonator. Matching is achieved by

Table 1. Domain Inversion–Inducing Methods

1. Inward–Ti Diffusion Method
   - Formation of a Ti coating 50~300 Å in thickness on +z plane
   - A heat treatment lasting for a few tens of minutes at temperatures ranging from 1,000~1,100°C
   - Occurrence of a domain inversion with Ti's diffusion inward to a depth of a few micrometers

2. Outward LiO_2 Diffusion Method
   - Quenching of LN after heating it at temperatures ranging from 1,050~1,100°C
   - Diffusion of LiO_2 outward and occurrence of a domain inversion on the +z plane
   - No inversion in the portion coated with SiO_2 layer

3. SiO_2–Loaded Heat–Treatment Method
   - Coating of the +z plane of LN with SiO_2 to a thickness of 1,000 K
   - Heat treatment at 1,000°C for a duration ranging from 1~2 hours
   - Diffusion of LiO_2 and occurrence of a domain inversion

4. Proton Exchange Heat–Treatment Method
   - Proton exchange on the −z plane of LT at 260°C using pyrophosphoric acid
   - A heat treatment at temperatures ranging from 500~600°C and occurrence of a domain inversion

5. Pyroelectric Field Method
   - Heating at 400°C by attaching a pair of metallic electrodes on the y plane of LN
   - Generation of a high voltage between the electrodes caused by pyro effects and occurrence of a domain inversion in the z direction

6. Electron Beam Radiation Method
   - Scanning the −z plane by grounding the z plane of LN and LT
   - Electron beam, up to 0.3 mA, 25 kV
   - Possible to cause a bulk–type domain inversion

comparing the frequencies of the light bouncing back from the $KNbO_3$ resonator with the semiconductor laser light at the comparison electronic circuits to generate feedback signals. The system is capable of outputting 41 mW of laser light against an input of 105 mW at a wavelength of 428 nm (conversion efficiency η = 39%). With a further reduction of system size, this method will be used more commonly along with the pseudo–phase matching method.

KTP crystal is of interest because it has very large incident light angularity as well as temperature tolerances and it can be grown easily compared to other

types of crystal. The drawback of the crystal is that it has a nonlinear optical coefficient about a quarter of the value of $KNbO_3$ and thus blue light cannot be generated by the angle-matching method. However, recently a successful generation of the second harmonics by the pseudo-phase matching method has been reported.[10] Using this method, KTP crystal is capable of generating lights up to the wavelength of blue light. Experiments using an 0.85 μm wavelength semiconductor laser produced a 2 mW blue light by inputting a laser beam into a KTP device having a length of 5 mm and a domain cycle of 4 μm. Compared to $LiNbO_3$, KTP has better laser-light-damage-withstanding capability and good temperature characteristics. These advantages make KTP suitable for generating blue light by the pseudo-phase matching method. Also, KTP crystal, a bulk-type domain inversion can be obtained through chemical reaction only.

KTP crystal is also being used to fabricate the internal resonator devices for generating the second harmonics. In these devices KTP crystal is used by being inserted into the laser resonator. This makes it possible to generate a strong electric field within the resonator easily and realize a high wavelength conversion efficiency. In addition, the use of KTP crystal makes it possible to obtain the TEM_{00} mode easily even when the special pattern of the semiconductor laser beam is not in good condition. By inserting a KTP piece and a $\lambda/4$ output stabilizing plate into an Nd:YAG laser resonator, a continuously generated green light with an output of 1 W has been obtained.[15] In addition, by inserting a KTP piece into the resonator of a 1 mm thick $Nd:YVO_4$ laser microchip, a green light (0.53 μm) with an output of about 10 mW has been generated in a single mode against the laser-exciting power of 760 mW.[16] This will make it possible to reduce the system size greatly and to obtain a single mode light in both vertical as well as horizontal directions.

3. Organic Nonlinear Optical Materials

In recent years active research has been conducted to develop organic nonlinear optical materials, and in Japan many low-molecular weight organic materials displaying nonlinear optical effects higher than that of KTP crystal have been developed. Those organic materials and products currently being developed include low-molecular weight crystals.[17] The disadvantages of these organic materials are their comparatively low material stability and the difficult of processing because of material softness.[18] Efforts to apply them to device fabrication have yet to come.

4. Future of the Nonlinear Optical Material Crystal Development Effort

Considering that a variety of wavelength-variable solid-state lasers, including semiconductor lasers and Ti:sapphire lasers, have been developed to cover a wavelength band ranging from red light to near-red light, there should be no need to divert nonlinear wavelength conversion devices to the red band applications. However, for infrared range applications, mainly for measurement, with the wavelength involved longer than 2 μm, the usefulness of parametric oscillators fabricated using KTP, $LiNbO_3$, and other nonlinear optical substances would increase. KTP crystal is the most suitable for generating green light. BBO and LBO crystals are regarded to be the most

suitable for generating pulsating blue-to-ultraviolet range lights. Efforts are under way to develop smaller, longer-service-life devices capable of continuously generating ultraviolet light by combining these crystals and solid-state lasers.

Research for generating blue light through the wavelength conversion of semiconductor lasers may be focused on the refinement of the pseudo-phase matching method by using the crystals of $LiNbO_3$, $LiTaO_3$, and KTP. Continued efforts must be made to understand the mechanism of the occurrence of domain inversion better by studying the crystal structure. To promote the practical utilization of $LiNbO_3$, light damage-withstanding capability must be improved, and in $LiTaO_3$ the technology to grow optically higher quality crystal must be established. Concerning optical devices, efforts must be made to develop easier-to-use bulk-type devices, in addition to waveguide-type pseudo-phase matching devices. To achieve this, it is important to establish a domain inversion technology that will make it possible to achieve high-efficiency wavelength conversion at lower conversion loss.

References

1.   Sasaki, T., LASER RESEARCH, Vol 17, 1989, p 804.

2.   Ibid., Vol 18, 1990, p 599.

3.   Sasaki, T. and Yokotani, A., J. CRYSTAL GROWTH, Vol 99, 1989, p 820.

4.   Yoshida, K., et al., Collection of papers prepared for 52nd Applied Physics Society meeting, Autumn 1991, 9a-M-8.

5.   Miyamoto, A., et al., Collection of papers for 14th annual meeting of Laser Society held at Tokai University, Feb 1992, 12a-II-1.

6.   Itoh, K., et al., J. CRYSTAL GROWTH, Vol 106, 1990, p 728, Vol 114, 1991, p 676.

7.   Kato, R., LASER RESEARCH, Vol 18, 1990, p 3.

8.   Fan, Y.X., et al., IEEE J. QUANT. ELECTR., Vol 25, 1989, p 1196.

9.   Chen, C.T., et al., J. OPT. SOC. AM., Vol B6, 1989, p 616.

10.   Sasaki, T., LASER RESEARCH, Vol 19, 1991, p 662.

11.   Yamamoto, Y., et al., CLEO'91, 1991, p CPD23.

12.   Seihara, T., Polymer Society meeting: "Latest Development in Organic Nonlinear Optical Materials," Nov 1991.

13.   Ito, H., et al., ELECTRO. LETTERS, Vol 27, 1991, p 1221.

14. Kozlovsky, W.J., et al., APPL. PHYS. LETTERS, Vol 56, 1990, p 2291.

15. Oka, M., et al., CLEO'90, p CWC5.

16. Sasaki, T., et al., OPT. LETTERS, Vol 16, 1991, p 1665.

17. Sasaki, T., OPTRONICS, Mar 1990, p 119.

18. Sasaki, T. and Namba, Y., OPTICS, Vol 21, 1992 (scheduled to be published in May.

Development of Ultra-Ion-Conductive Glass, New Ultra-Ionic-Conductive Hybrid Material

[Article by Tsutomu Minami, Osaka Prefectural University Department of Engineering]

[Text] The three pillars propping up the high technology community today are said to be biotechnology, information, and high performance materials. The reason for materials development drawing such high attention is that it has now been recognized widely that genuine technological innovations can be promoted by the development of high-performance materials.

Glass is one of these materials. Extensive research has been conducted to develop new functional glass, including glass fibers for optical communications. The ultra-ion-conductive glass that will be introduced in this paper is another such glass product.

Table 1. Comparison of Electric Conductivity Between Ultra-Conductive Glass and a Few Other Substances

	Electric conductivity/S cm^{-1} (25°C)
5% NaCl solution	6×10^{-2}
5% AgNO$_3$ solution	2×10^{-2}
75AgI·25Ag$_2$SeO$_4$ glass (mol%)	2.2×10^{-2}
Soda lime glass[*]	3×10^{-13}

  [*] 73% SiO$_2$, 16% Na$_2$O, 5.5% CaO(wt%), and also including MgO, Al$_2$O$_3$, and K$_2$O

Commonly, glass is regarded as an electrical insulator. However, contrary to common knowledge, glass that conducts electricity very well has been developed. As listed in Table 1, 75Agl·25Ag$_2$SeO$_4$ glass displays an electric conductivity at 25°C, that is by more than 10-digits-worth higher than that of conventional soda-lime glass. ??conductivit of the advanced glass is almost at the same level with that of 5%NaCl solution and 5%AgNO$_3$ solution. This tells that the above common knowledge, glass as insulator is now scientifically groundless.

Glass exhibiting an ion conductivity as high as that of electrolytic solutions is called "ultra-ion-conductive glass." This name was adopted considering that "ultra-ion conductive" in many cases refers to a crystal displaying high ion conductivity.

This paper will touch on methods to produce high ion conductivity in solid-state materials, the results of comparison of ion conductivity between glass and crystals, the examples and the reason for glass displaying generally higher ion conductivity than crystals (the merit of vitrification), examples of newly developed high-ion-conductive glass, and the example of the successful development of a novel hybrid material by freeze confining α-Ag1—a material that displays ultra-ion-conductive glass under high temperature—within glass at room temperature. This paper will also refer to the mechanism of ion conduction, the relationships between the electron configuration in ion and the conductivity, the relationships between the ion-mixing effects and the conductivity, and glass structure.

Ultra-Ion-Conductive Glass

In the field of electronics, today's prosperity in the industry has been realized as a result of solid-state material (transistor) replacing gas-filled parts (vacuum tube), leading to an improvement in the reliability and smaller size of electronic systems. While in the field dealing with ion-conductive materials, fluid-form electrolytes still play a major role and the development of solid-state counterparts has made not much progress. Because of this, active efforts have been made to develop solid-state electrolytes (ultra-ion conductors).

1. Improvement of Ion Conductivity in Solid-State Substance

An ion has an electric charge and has a considerably large radius and mass. This makes it difficult for an ion to move around within a solid-state substance. So the phenomenon of ion conductivity is observed only when the required conditions are satisfied.

The following three conditions are well known.[1,2]

(1) Presence of Lattice Defects

When CaO was added to ZrO_2, bivalent Ca takes up the positions for quadrivalent Zr electrons. This disturbs the electric neutrality, generating the lattice defects of oxygen. This causes oxygen ions to move.

(2) Presence of a Special Crystal Structure

β-alumina assumes a laminar crystal structure having an $Na_2O \cdot 11Al_2O_3$ structure. Bonding between the adjoining layers is weaker than the bonding within the layer. Na^+ ions present between these layers can thus move around comparatively easily. There is also a structure called horandite [phonetic] existing within a crystal that serves as a tunnel for easy movement of ions through it.

42

(3) Presence of a Balanced Structure

This can be considered as a variant of the above case of special crystal structure. However, this differs from the case considerably, so it will be handled as an independent structure. For example, α–AgI has a crystal structure in which I⁻, having a large ion radius, forms a body–centered cubic structure with two I⁻ ions present within each of the unit lattices. In order to satisfy the AgI stoichiometry, the same number of Ag^+ ions must be present.

There are 12 equivalent places for those Ag^+ ions. The fact that these ions are not immobilized at specific places but are distributed in a statistically balanced mode makes Ag^+ ions capable of moving around just like they are in a solution.

2. Merits of Vitrification

The above three represent the methods for obtaining high–ion conductivity from crystallized substances. Recently, a fourth method has been found in which high–ion conductivity can be obtained from amorphous or vitrified substances. Compared to crystals, ions are believed to move around ore easily within glass that has less tight structure than crystal.

Figure 1[3] gives a comparison of ion conductivity between crystallized glass and $AgI–Ag_2O–P_2O_5$–system materials. Over the entire composition range, crystallized glass displays conductivities 5~20 times higher than their counterparts.

In the case of electron–conductive substances, making the substances into an amorphous state causes a decline in the conductivity because the electrons or holes are scattered violently by the lattice vibration. However, in the case of ions, conductivity improves by promoting the change into an amorphous state (vitrification), as is clear from Figure 1. In addition to these features, vitrification produces a number of other advantages as given in Table 1.[4] Considering these advantages, the importance of glass and other amorphous materials in the development of ion–conductive material will increase in the future.

In many cases, a term "ultra–ion conductor" denotes a substance in a crystallized form. In order to differentiate from this clearly, glassy substances are commonly called "ultra–ion–conductive glass" or "high–ion–conductive glass."
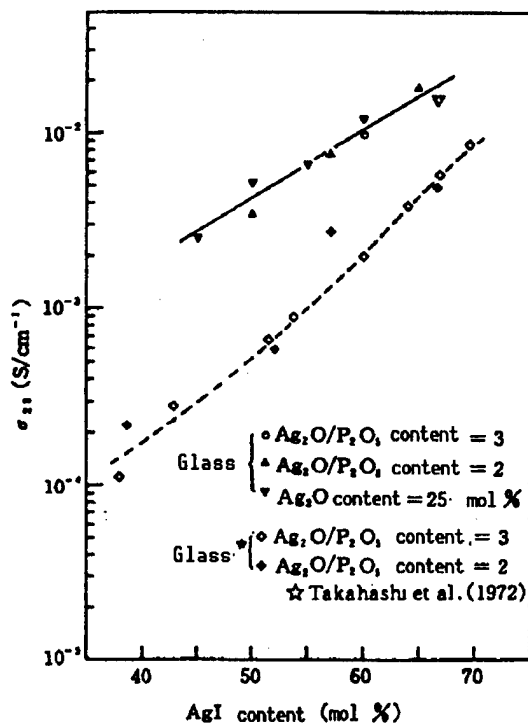

Figure 1. Comparison of Ion Conductivity Between AgI–Ag₂O–P₂O₅–System Crystals and Same–System Glass at 25°C (Cited from Ref. 3 material)

3. Development of New Glass Synthesizing Material Systems

Items 6 and 7 features of vitrification as described in Table 1 will be elaborated below with the help of Table 2.[5] Table 2 lists four ion types—Ag^+, Li^+, Cu^+, and Na^+—as movable ions. Among these, research has most progressed on Ag^+ ion. However, recently emphasis is shifting toward Li^+ ion. Those items in the table are listed as glass-formation material systems and they do not represent the chemical compositions of glass. They are the most representative systems and many other variations are available (Table 1[6]).

Table 1 [as published]. Advantages of Vitrification (cited from Ref. 4)

(1) Realization of high-ion conductivity
(2) Homogeneity, isotropy
(3) No grain boundary
(4) Good moldability
(5) Ease in forming thin film
(6) Availability of many glass formation material systems
(7) Ease in controlling characteristic value with availability of wide-ranging chemical composition

Table 2. Ion Conductivities in a Number of Kinds of Ion-Conductive Glass (cited from Ref 5)

Movable ion	Glass formation material systsem	Ion conductivity (S/cm, 25°C)	Reference number
Ag^+	$AgI-Ag_2O-MoO_3$	$10^{-4} \sim 10^{-2}$	6
	$AgI-Ag_2O-P_2O_5$	$10^{-4} \sim 10^{-2}$	3
	$AgI-Ag_2O-B_2O_3$	$10^{-6} \sim 10^{-2}$	7
	$AgI-Ag_2-SeO_4$	$10^{-4} \sim 10^{-2}$	8
Li^+	$LiI-Li_2S-B_2S_3$	$10^{-4} \sim 10^{-3}$	9
	$LiI-Li_2S-P_2S_3$	$10^{-4} \sim 10^{-3}$	10
	Li_2S-GeS_2	$10^{-7} \sim 10^{-5}$	11
	$Li_2O-LiCl-B_2O_3$	$10^{-7} \sim 10^{-5}$	12
	$Li_2O-SiO_2-ZrO_2$ thin film	$10^{-8} \sim 10^{-6}$	13
	$Li_2SiO_4-Li_3PO_4$ thin film	$10^{-6} \sim 10^{-4}$ (200°C)	14
Cu^+	$CuI-Cu_2O-P_2O_3$	$10^{-7} \sim 10^{-3}$	15
	$CuI-Cu_2O-MoO_3$	$10^{-3} \sim 10^{-2}$	16
Na^+	$Na_2O-ZrO_2-P_2O_5-SiO_2$	$10^{-6} \sim 10^{-5}$ (150°C)	17,18

As for these material systems, they have their individual compositional ranges that make it possible to form glass. However, the availability of many kinds of material components allows making glass having greater varieties of the chemical composition than its crystal counterparts (Table 1[7]).

This paper will describe Ag^{+} ion–conductive glass first, followed by a description of Li^{+} ion–conductive glass. In addition, a reference to Cu^{+} ion–conductive glass will be made in the section on ion–conducting mechanism.
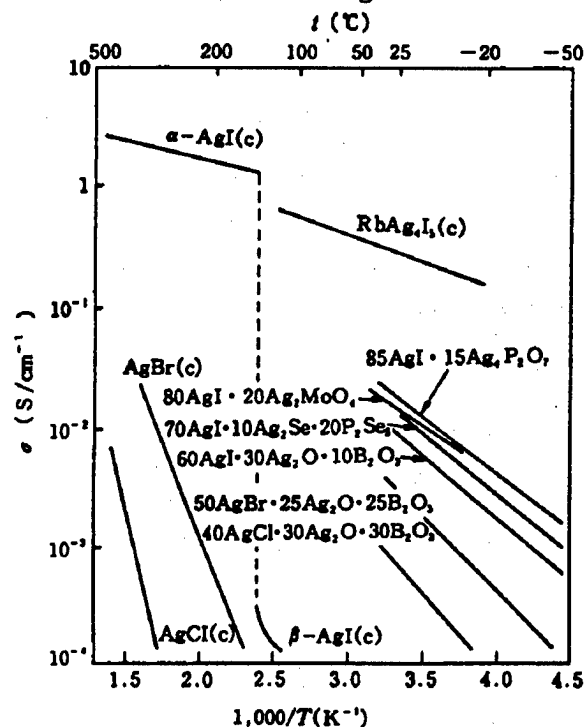
3.1 Ag^{+} Ion-Conductive Glass

Figure 2[19] shows the temperature dependence of ion conductivity in some of the Ag^{+}-system ultra–ion–conductive glass. For comparison, the data on the temperature dependence of several types of crystallized substances are also shown in the figure (those attached with a mark "(c)"). Among these, RbAg$_4$I$_5$(c) is one solid–state ion conductor and has a very large room temperature conductivity of 2 x 10^{-1} S/cm. (The largest value attained to date stands at 4.7 x 10^{-1} S/cm[20] realized in a Rb$_4$Cu$_{16}$I$_7$Cl$_{13}$ compound in which part of the Rb was displaced with K.)

To avoid the figure becoming overcrowded, only the data for the most representative types of glass are shown. It can be seen that comparatively high conductivities are exhibited not only by AgI glass, but also by AgBr and AgCl glass. At temperatures higher than 146°C, AgI crystal exists as α–AgI, and displays very high–ion conductivity.

For comparison, the data of several types of crystallized counterparts are also shown by being distinguished with a mark (C) from other noncrystallized ones.

Figure 2. Temperature Dependence of Conductivity in Typical Ion-Conductive Glass
(Cited from Ref 19 material)

The reason for glass containing AgI exhibiting high–ion conductivities can be explained by such high–ion conductivity level of α–AgI. However, AgBr crystal and AgCl crystal do not contain a phase displaying such a high–ion conductivity as α–AgI, and they have low conductivities as shown in the figure. As shown above, other components making up these glass, too, have very low–ion conductivities as individual components. The fact that they display high–ion conductivities when they have been vitrified serves as another example of the merit of vitrifying them in the development of high–ion–conductive materials.

As far as ion–conductive values in Table 2 are concerned, Ag ion–conductive glass systems have almost the same values with Li^{+} systems. However, the number of papers published covering the research on the former is far larger than the latter, indicating the former has been researched more extensively. The reason for this is that Ag^{+} glass is easier to process, is stable at room temperature, and has higher ion conductivity.

The basic Ag$^+$ ion-conductive glass is composed of AgI–Ag$_2$O–M$_m$O$_n$–system substances (M$_m$O$_n$ denotes various types of oxides). There are many kinds of M$_m$O$_n$, and each of these glass material systems has a comparatively wide glass formation condition range. This allows much freedom in determining glass composition in developing ion-conductive glass.[8] It is known that ion-conductive glass can also be made by displaying I and O with other VII group or VI group elements, as described in Figure 3.[4,21] This diversity in the glass formation material system has contributed greatly to the research on the structure of Ag$^+$ ion-conductive glass and the ion-conducting mechanism.
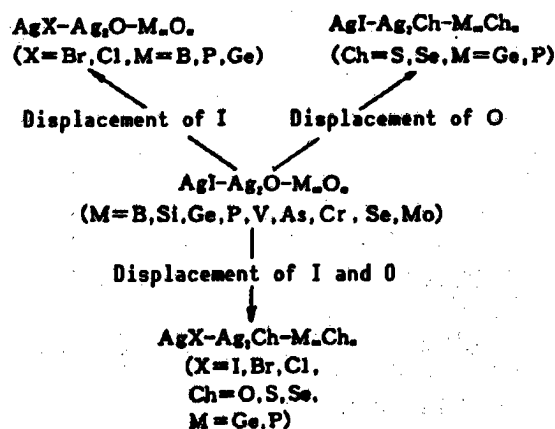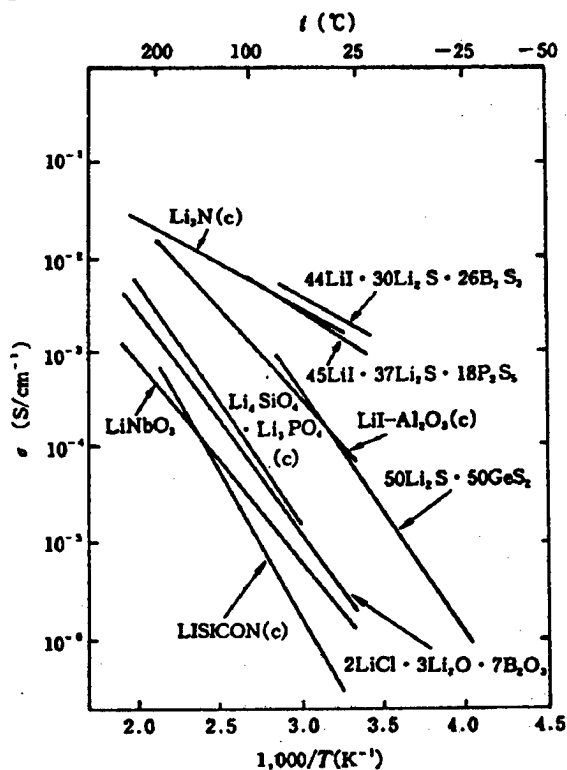
AgX–Ag$_2$O–M$_n$O$_n$ AgI–Ag$_2$Ch–M$_n$Ch$_n$
(X=Br,Cl,M=B,P,Ge)   (Ch=S,Se,M=Ge,P)

Displacement of I   Displacement of O

AgI–Ag$_2$O–M$_n$O$_n$
(M=B,Si,Ge,P,V,As,Cr,Se,Mo)

Displacement of I and O

AgX–Ag$_2$Ch–M$_n$Ch$_n$
(X=I,Br,Cl,
Ch=O,S,Se,
M=Ge,P)

Figure 3. Expansion of Glass Formation Material Systems by Displacing I and O in AgI–Ag$_2$O–M$_m$O$_n$ Systems
(Cited from Refs. 4, 21 materials)

t (℃)

For comparison, the data of several crystallized counterparts are also shown by being distinguished with a mark (c) from those noncrystallized ones.

Figure 4. Temperature Dependence of Conductivity in Typical Li$^+$ Ion-Conductive Glass
(Cited from Ref. 19 material)

3.2 Li$^+$ Ion-Conductive Glass

Figure 4[19] shows the temperature dependence of ion conductivity for the most representative of Li$^+$ ion-conductive glass listed in Table 2. compared to Ag$^+$ counterparts, the number of glass types available is comparatively fewer and the conductivity attained is considerably lower. The conductivity values for the LiI–Li$_2$S–B$_2$S$_3$ system and LiI–Li$_2$S–P$_2$S$_5$ system glass are the highest attained to date as Li$^+$ ion-conductive glass.

Figure 4 also shows the data for a few types of crystals (carrying a mark "(c)" for comparison. Among these crystals, Li supersonic conductor (LISICON) is a representative Li$^+$ ion conductor and its chemical composition is expressed as Li$_{14}$Zn(GeO$_4$)$_4$.[22,23] The Li$_4$SiO$_4$–Li$_3$PO$_4$–system forms solid solutions and ion conductivity in the system peaks at 1:1 mol ratio between the two components.[24] In Li$_3$N, conductivity decreases when its purity improves, and high conductivity is measured when moisture is present within the material. One of the problems in Li$_3$N includes its low stability in the air.[25]

46

In glass, it is difficult to achieve high-ion conductivity by using high purity oxides. Attempts have been made to improve Li^+ ion conductivity by using lithium halide-containing material systems of sulfides instead of using oxide systems. These material systems must be handled carefully because they are unstable in the air. On the other hand, efforts are being made to use currently available material systems by processing them into thin films to reduce the apparent resistance value in these systems.

3.3 Ultra-Rapid Cooled Glass

As described above, it is difficult to develop high-ion conductivity in oxide-system materials through conventional techniques. Attempts are being made to increase conductivity in Li^+ ion-conductive glass by cooling the material at ultra-rapid cooling speeds. Current efforts were prompted by the data released by the Bell Laboratory of the United States in 1977, that is shown in Figure 5.[26] The figure indicates the temperature dependence of the dielectric constant in lithium niobate glass that can be produced by cooling $LiNbO_3$ at ultra-rapid cooling speed. The ordinate axis gives the dielectric constant (ϵ) values and the abscissa axis testing temperature (K). In general, crystallization of a substance causes the dielectric constant of it to shrink greatly. However, in ultra-rapid cooled lithium niobate glass, the dielectric constant reaches a very high value, in the order of 10^5. In the glass, another dielectric constant peak appears before the material crystallizes. Finding these double peaks attracted great attention when it was reported that the double-peak feature shows the possibility of the material exhibiting a phenomenon similar to a ferroelectric dislocation, despite the fact it assumes an amorphous glass state.
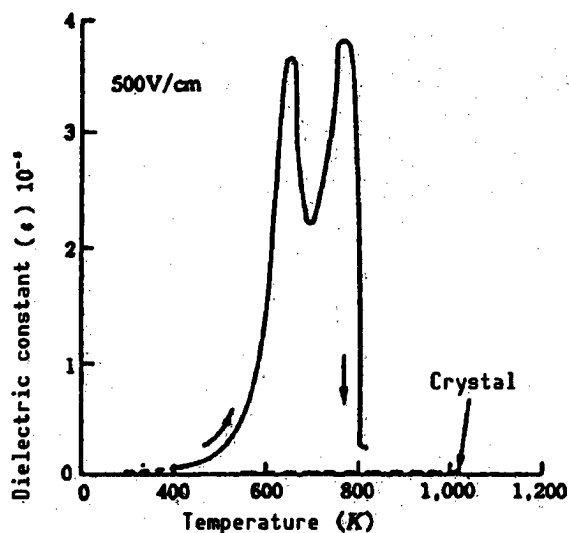

Figure 5. Temperature Dependence of Dielectric Constant in $LiNbO_3$ Glass (Cited from Ref. 26 material)
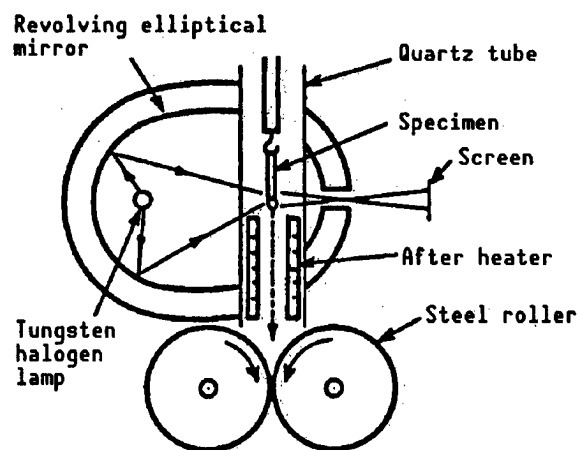

Figure 6. Ultra-Rapid Cooling System Combined an Infrared Light-Focused Furnace and Twin Rollers (Cited from Ref 27 material)

Encouraged by this report, this author and other researchers have attempted to produce oxide glass using the ultra-rapid cooled technique. Figure 6[27] gives

47

the schematic representation of the cooling system. In the system, a temperature of 1,800°C can be generated by focusing the light from a tungsten halogen lamp placed within an elliptical mirror. That temperature can be obtained in a few seconds after the lamp is turned on. As test specimens, the sintered compacts of the mixture of material powders with the composition adjusted to desired compositions were used. The system makes use of no crucible and the melting conditions can be adjusted somewhat by changing the environment within the quartz tube. The system allows for observation of the melting condition through a lens. Increasing the temperature brightens the inside of the tube.

This author has conducted experiments to confirm the data given in Figure 5. Lithium niobate ($LiNbO_3$–$50Li_2O\cdot50Nb_2O_5$) is a material that is very difficult to vitrify. So to promote vitrification, 5% barium oxide was introduced by keeping the mol ratio of Li_2O and Nb_2O_3 at a constant level. Figure 7[28] gives the characteristics of temperature vs. dielectric constant and ion conductivity of the glass thus produced. The glass achieved a very high dielectric constant (Δ value reaching to an order of 10^5). However, crystallization caused the constant to shrink to a very low level. This caused the specimens to display a conspicuous peak in the value of the dielectric constant. However, no twin peaks as were observed in the above instance of $LiNbO_3$ were observed in this author's experiment. The ion conductivity (o) in the specimens displayed a change pattern that was quite similar to that of dielectric constant, and the value plummeted by an order of about 10 digits as a result of crystallization. From these results in which the dielectric constant and ion conductivity exhibited almost the same temperature–dependence patterns, it is believed that these phenomena do not indicate the manifestation of ferroelectric characteristic caused by ultra–rapid cooling, but the appearance of an apparently large dielectric constant caused by the polarization of the ions induced by ion conduction.

Figure 7. Temperature Dependence of Dielectric Constant and Ion Conductivity in Ultra–Rapidly Cooled Glass (Cited from Ref. 28 material)

Figure 8[29] shows the changes of ion conductivity (500 K) when a number of kinds of third–material components were introduced into $Li_2O\cdot M_xO_y\cdot Nb_2O_5$–system glass. It can be seen that conductivity increases exponentially as the content of Li_2O increases, though there are fluctuations in the conductivity value amounting to an order ranging from one to two digits of value depending on the kind of
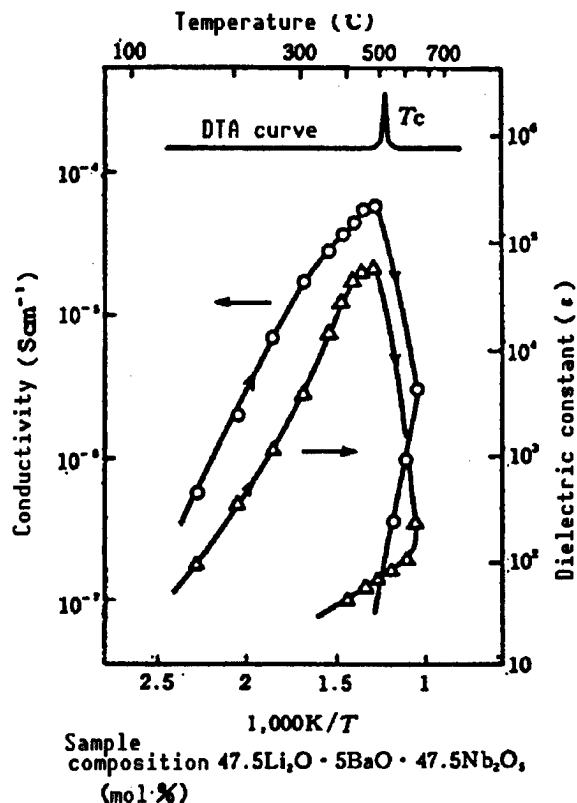
48

Figure 8. Compositional Dependence of Ion Conductivity (500 K) in $Li_2O-N_xO_y-Nb_2O_5$-System Ultra-Rapidly Cooled Glass (Cited from Ref. 29 material)

Figure 9. Compositional Dependence of Ion Conductivity in Li_4SiO_4-Li_3BO_{34}-System Ultra-Rapidly Cooled Glass (Cited from Ref. 31 material)

third component introduced. This indicates that ion conductivity in the glass is dictated by the content of Li_2O. So in order to improve conductivity, Li_2O content must be increased. This may cause deterioration in the strength of glass when producing a glass having a very high-ion conductivity.

However, the relationships between material composition and ion conductivity are not so simple, as indicated in Figure 9.[30,31] The figure shows the compositional dependence of ion conductivity in a glass composed of lithium orthosilicide (Li_4SiO_4) and lithium orthoboride (Li_3BO_3). The ion conductivity peaks at a specific composition. In this system of glass, lithium represents the only cations involved, however, as anion, two different substances are contained—orthosilicide and orthoboride. It is believed that the peak in ion conductivity resulted from mixing of two different anions, with a phenomenon known commonly as "mixed-anion effects" occurring.

4. Ion Conduction Mechanism

Generally, ion conductivity in glass can be calculated from an equation,

$$\sigma = ne\,\mu \tag{1}$$
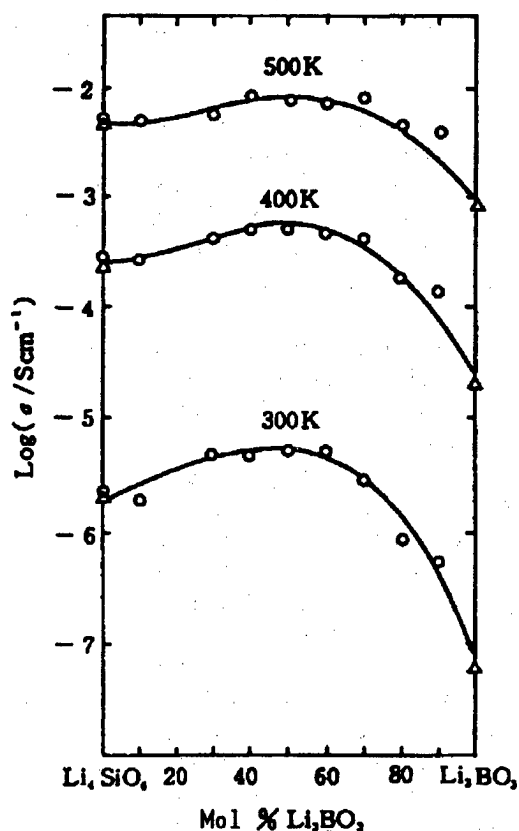
49

where n denotes charge carrier, e electric charge, and μ the mobility. The value of σ changes exponentially when the composition of a glass changes, as is clear from Figure 2. The important thing in discussing the ion conduction mechanism in glass is to clarify the mechanism causing the change of the conductivity when glass composition changes, and whether some of the movable ions within glass or all of them are contributing to the manifestation of the conductivity as charge carrier. (Through experiment it has been confirmed that almost all the glass discussed in this paper are ion conductors in which electrons play little role in promoting ion conductivity.)

As for the conduction mechanism, three conduction models have been proposed: 1) the random-site model[32,33] focusing on the change of μ value, 2) the weak-electrolytic model[33,34] taking into account the change of n value, and 3) the diffusion-channel model[8,19,35] combining the change of n and μ value (Table 3).

Table 3. Ion-Conduction Mechanisms for Three Condition Models

Model	Density n	Density μ	Density σ
Random site model	All cation (change by the composition being small)	Changes greatly depending on the composition	Value of σ dictated by change of μ
Weak electrolytic model	Part of cation (equivalent to dissociated cation)	At a constant level irrespective of compositional change	Value of σ dictated by change of n value
Diffusion channel model	Part of cation	Changes depending on compositional change	Value of σ affected by change of both n and μ

In the random-site model, all types of ions, such as Ag^+ and Li^+ that have the possibility of contributing to ion conduction function as charge carrier. Also, the activation energy has a distribution pattern in which the energy level varies from site to site, causing change of the mobility depending on the change of the composition reflecting the difference of energy level. In general, the change of ion density caused by changing the composition is small. So the change of conductivity caused by the compositional change is dictated by the change of the mobility.

In the weak-electrolytic model, all those ions that have the possibility of improving conductivity do not serve as charge carriers. Like the situation within weak electrolytic solutions, a small portion of the cations dissociates to generate ions that contribute to ion conduction. In the model, mobility remains at a constant level not affected by the composition. This means that the change of conductivity associated with the change in composition is dictated by the density of the dissociated ions (density of charge carrier).

50

The diffusion-channel model assumes that diffusion channels for movement and diffusion of ions exist within glass. The length of these channels determines the degree of mobility, and the condition of the channels is believed to change depending on the composition and structure in a glass. Among those ions, the ones that are located in the diffusion channels only function as the charge carrier. Considering that part of cations contributes to the improvement in conductivity and mobility changes when the composition in a glass changes, it is believed that the change of conductivity when there is a change in composition is affected by both the density of the dissociated ions and the mobility.

At present, it is not known yet which of these models is most suitable to explain the conduction mechanism. However, the diffusion-channel model proposed by this author's group is gaining increasing support.

The structure model shown in Figure 10[36] may give a clearer idea of this model. (This structure model will be detailed in the next section.) The structure model is for AgI–Ag$_2$MoO$_4$–system glass. The triangles represent MoO$_4{}^{2-}$ tetrahedron ions, the circles filled with oblique lines, I ions, and the smaller circles, Ag$^+$ ions. Compared to the irregular three-dimensional mesh structure of conventional glass, the structure shown in the figure is unique.
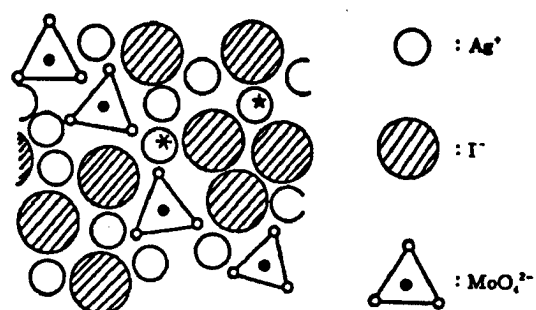

Figure 10. Structure Model of AgI–Ag$_2$MoO$_4$–System Glass
(Cited from Ref. 36 material)

In the structure model, it can be seen that there are two types of Ag$^+$ ions—an Ag$^+$ ion positioned close to an oxygen ion and an Ag$^+$ ion surrounded with iodine ions. It is believed that the latter plays an important role in ion conduction with these Ag$^+$ ions moving along the diffusion channels formed by iodine ions.

There is one more important problem in considering the ion-conduction mechanism.

As may be surmised from Table 2, there are many Ag$^+$–system substances whose conductivity reaches 10^{-2}S/cm^{-1}. However, in an Li$^+$ system, none have such a high conductivity, with only a few substances displaying a value of 10^{-3}S/cm^{-1} at the highest. In an Na$^+$ system, the conductivity is far smaller. A comparison of ion conductivity among these three types of glass having similar chemical compositions showed that there are the following conductivity relationships among them: $\sigma(\text{AgA/cm}^2) > \sigma(\text{Li}^+) > \sigma(\text{Na}^+)$. Considering the radius of those ions listed in Table 4, this order of conductivity is worth nothing. That is, an Ag$^+$ ion having a radius about twice that of an Li$^+$ ion exhibits a conductivity that is far larger than that of its Li$^+$ counterpart.

Two reasons may contribute to the large-radius Ag$^+$ ions displaying the highest conductivity.

51

Table 4. Ion Radius and Electron Configuration in a Univalent Cation

Ion	Radius/A	Electron configuration
Ag^+	1.26	[Kr shell]$4d^{10}$
Cu^+	0.96	[Ar shell]$3d^{10}$
Li^+	0.68	[He shell]
Na^+	0.97	[Ne shell]

The first assumption is that there is a relationship between the ion radius and the structural gap dimension that contributes to the movement of Ag^+ ions. Among various types of β–Al_2O_3, it is well known that $Na^+\beta$–Al_2O_3 displays the highest conductivity.[37] It is explained that such high conductivity is realized because of the presence of an appropriate relationship between the ion radius and the gap dimension. It is believed that similarly high conductivity could be measured in other types of glass of similar material systems.

The second assumption attributes the high conductivity to the electron configuration in Ag^+ ions. As described in Table 4, Ag^+ takes d^{10} in electron configuration in the outermost orbit. While Li^+ and Na^+ take a rare–gas structure such as s^2 and s^2p^6. The assumption assumes that the d orbit's lower screening capability of nuclear charge compared to that of the s orbit and the p orbit and the softer orbit makes Ag^+ ions easier to move around prompted by small shocks caused by collision with the lattice when they move through the gaps.

In β–Al_2O_3 crystal it is believed that the sturdy crystal lattice secures a structural gap that is suitable for the ions to move around. In amorphous substances such as glass and those in solution form, it is commonly known that in principle smaller ions are easier to move around. All in all, it is difficult to explain ion conduction mechanisms by the first assumption. There is a high possibility that ion radius and ion electron configuration play important roles, as described in the second assumption.

Figure 11[16] shows the compositional dependence of ion conductivity (25°C) in AgI–Ag_2MoO_4–system and CuI–Cu_2MoO_4–system glass. As is shown in the figure, Cusystem glass displays a higher conductivity among the two similar material system glass. Considering the fact that Cu^+ ions have the d^{10} structure, the structure the same as Ag^+ ions, and have a smaller ion radius than that of Ag^+, the results
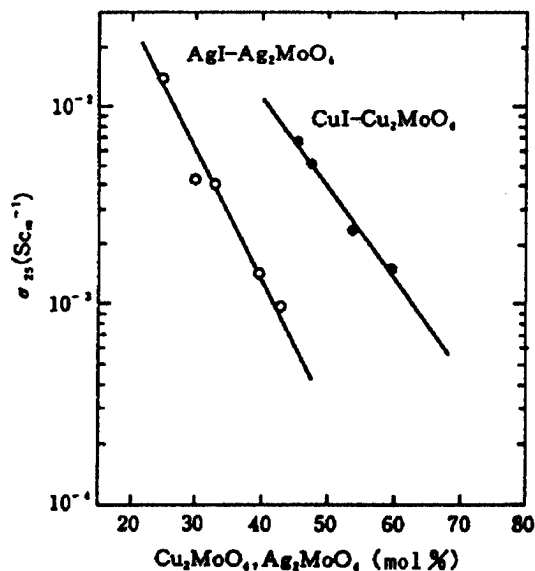

Figure 11. Compositional Dependence of Ion Conductivity (25°C) in CuI–Cu_2MoO_4–System Glass and Ag_2MoO_4–System Glass
(Cited from Ref. 16 material)

shown in the figure seem to demonstrate the validity of the second assumption. That is, in order to obtain high-ion conductivity in glass, the ion radius must be small and the electron configuration assumes the d^{10} structure, rather than the rare-gas structure.

To prove the validity of this conclusion, it is necessary to create many more Cu^+ ion-conductive glass specimens to obtain more objective data. However, there are a number of problems in doing this. The largest obstacle is the fact that the $CuI-Cu_2-MoO_4$ system,[16] $CuI-Cu_2O-P_2O_5$ system,[15] and $CuI-CuCl-RbCl$ system[38] are the only Cu^+ ion-conductive glass known to date, and at present they are difficult to produce. Another problem is the fact that in many cases, within glass, Cu is present in the form in which the univalent and bivalent forms coexist, rather than being present in univalent form only. (The condition of the coexistence deteriorates the ion conductivity greatly just as in the case of $Na_2O-CaO-SiO_2$-system glass.) Even if the glass can be created, the discrepancy in glass-formation ranges between the Ag system and Cu system makes it difficult to make direct comparison. In addition, there are substantial differences in the exponential terms associated with the conductivity's temperature dependence between the Ag system and Cu system,[16] and there may be differences in the conduction mechanism. There are still many research problems to be solved.

5. Glass Structure

This section will introduce typical examples of the infrared absorption spectrum and the Raman spectrum of Ag^+ ion-conductive glass. These spectrum conditions are closely related to the conduction mechanisms discussed above.

Figure 12[36,39] shows the infrared absorption spectra in $AgI-Ag_2O-MoO_3$-system glass. The chemical composition for each of these spectra is illustrated in the triangular diagram inserted in the figure. The spectra (a) to (d) exhibit the chemical compositions corresponding to an $Agi-Ag_2MoO_4$ pseudo-two component system, and the spectra (e) and (f) represent the chemical compositions that contain small amounts of MoO_3. In the spectra (a)~(b) the absorption of MoO_4^{2-} tetrahedron ions in v_3 and v_4 modes may be observed. In the spectra (e) and (f), the symmetrical as well as asymmetrical absorption in Mo-O-Mo binding caused by the condensation of MoO_4^{2-} in addition to the above absorption may be observed. Spectra (a)~(d) indicate that the glass is composed of isolated MoO_4^{2-} monomer ions, I^- ions, and Ag^+ ions, and the spectra (e) and (f) reveal that the glass additionally contains tiny amounts of
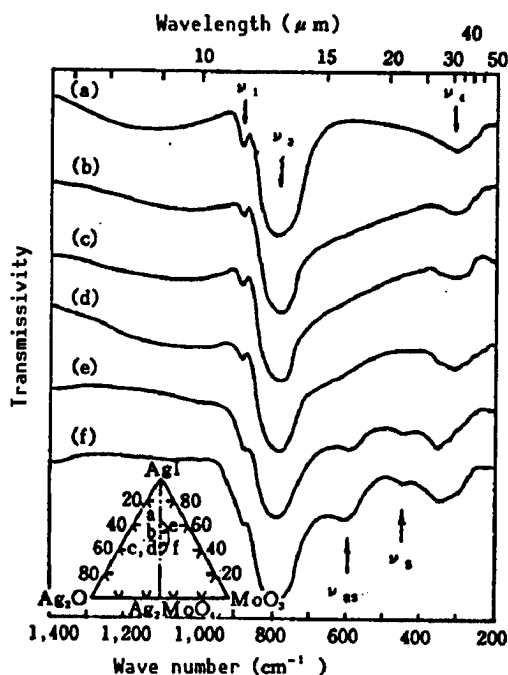

Figure 12. Infrared Absorption Spectra in $AgI-Ag_2O-MoO_3$-System Glass (Cited from Ref. 36, 39)

condensed anions. Spectra (c) and (d) are for glass that have the same chemical composition, but were created using different starting materials— AgI, Ag_2O, and MoO_3 for (c) glass and AgI, and Ag_2MoO_4 for (d) glass. The difference starting materials causes almost no difference between the two spectra. (The starting materials of (a) glass and (b) glass are the same as that of (c) glass.)

The glass structure shown in Figure 10 was drawn based on the results described above.

Experiments involving shifting of the absorption-band peak through ion exchanges with Ag^+ ions and K^+ ions have found that there is a considerably strong partial covalent binding between Ag^+ ions and the oxygen ions within MoO_4^{2-}.[36,39] In Figure 10, the Ag^+ ions (small circles with an asterisk within them) located close to MoO_4^{2-} ions are tightly bound with the oxygen ions within MoO_4^{2-} ions. The glass structure shown in Figure 10 has the features of the so-called ion glass. Conventional structure ion glass contains two types of cation and usually one of them is bivalent cation. It is said that vitrification occurs as a result of this cation interacting strongly with anions. Different from this conventional glass, the glass described above contains only Ag^+ ions as cation. The phenomenon of a strong, partially covalent, binding is believed to play an important role in the formation of glass. Moreover, this phenomenon is believed to be responsible for the presence of two types of Ag^+ ions—easily movable Ag^+ ions and not-easily-movable Ag^+ ions.

The infrared absorption spectrum provides information about the anion structure, but not about the structure around the Ag^+ ions. (the information about the surrounding structure can be obtained from the Raman spectrum.) Concerning this, an interesting result has been reported that is shown in Figure 13.[40,41] The spectra shown in the figure are those of $40AgX \cdot 60AgPO_3$ (mol%) glass. Here, X represents halogens, such as I, Br, and Cl. It is said that the spectrum band observed around 60 cm^{-1} represents a condition in which Ag^+ ions are surrounded by oxygen atoms (not-easily-movable Ag^+ ions), and the band ranging from 190~115 cm^{-1} in which a shift of spectrum peak is observed as a result of the change of halogen type represents the presence of AgX_4 (easily movable Ag^+). These Raman spectra data back up the diffusion-channel theory to explain the ion-conduction mechanism effectively.

Wave number (cm^{-1})

Spectra are presented in relative strength based on the ν_3PO_4 strength measured at 1,142cm^{-1}

Figure 13. Raman Spectra of $40AgX \cdot 60AgPO_3$ (mol%) Glass (Cited from Ref. 40 material)

6. Application Field

Ion conductors, including ion-conductive crystals, can be applied to ion censors, fuel cells, capacitors, solid-state batteries, and display materials. In connection with these application fields, this section will refer to
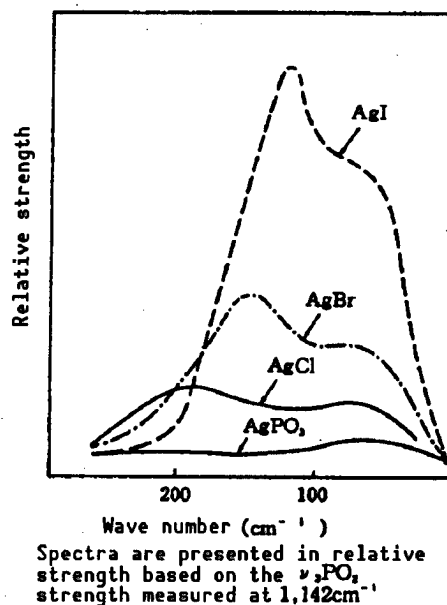
54

"electromechanism" and an instance of utilization as the cathode material in secondary batteries, as in the cases in which the problem of intercalation reaction is involved.

Figure 14[42] gives the electrochromism spectra for WO_3–Nb_2O_5–Li_2O–system ultra–rapid cooled glass. When univalent cations and electrons are injected simultaneously into a vapor–deposited amorphous WO_3 film placed under an electric field, M_xWO_3 is created as a result of the chemical reaction shown below:

$$xM^+ + WO_3 + xe \rightarrow M_xWO_3$$
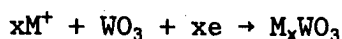
A blue substance is created by this reaction. Active research is under way to use the substance to create character/image display elements and as a material to control light strength. Addition of Li_2O to WO_3 causes a change in the response speed without affecting the color noticeably. However, introduction of Nb_2O_5 causes the peak of the spectrum to shift toward the low wavelength side as the added amount of the substance increases, as shown in Figure 14. This suggests that by proper selection of the third components introduced, it would be possible to produce multicolors.

Content of Nb_2O_5 increases from specimens No. 1 toward No. 5

Figure 14. Electrochromism in Li_2O–WO_3–Nb_2O_5–System Ultra–Rapidly Cooled Glass (Cited from Ref. 42 material)

The possibility of generating multicolors by applying an electric field in one polarity and making it disappear by applying in opposite polarity could produce display elements that have better performance than liquid crystal display elements. In addition, the electrochromic glass could be used in light–strength–adjustment applications.

In order to make this research bear fruit, effort must be made to develop superior ultra–ion conductors as ion supply sources and to develop electrochromic materials having better response and stability. Development of ultra–ion-conductive glass will contribute to these efforts.

The reaction occurring at the cathode (positive electrode) of the secondary batteries is similar to the one described by the above chemical–reaction equation in the formation of M_xWO_3. During the discharge period, a reducing reaction in the direction from the left side to the right side of the equation takes place, and an oxidizing reaction in the direction from the right side to the left side occurs during the period of recharging.
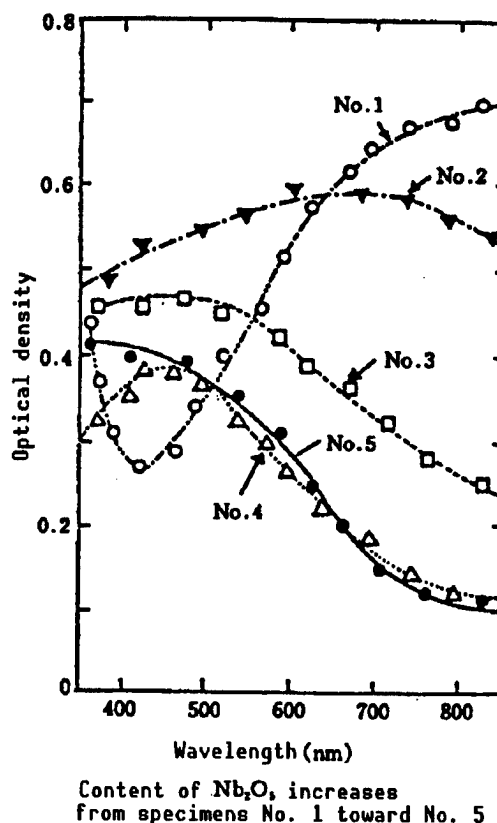
Active research has been conducted on the intercalation reactions in TiS_2 and MoS_2 having a laminar crystal structure. In recent years, however, attention is shifting to amorphous materials because it has been found that they can produce products of larger capacity and longer service life because of the smaller volume changes between discharge and recharge cycle.

To date a number of types of amorphous glass have been developed by introducing various types of components into V_2O_5 glass that was created by the ultra-rapid cooled technique. The characteristics of these are shown in Figures 15[43] and 16.[44] The battery whose data are shown in these figures is composed of $Li/1M$ $LiClO_4$–propylene carbonate/V_2O_5–system glass.
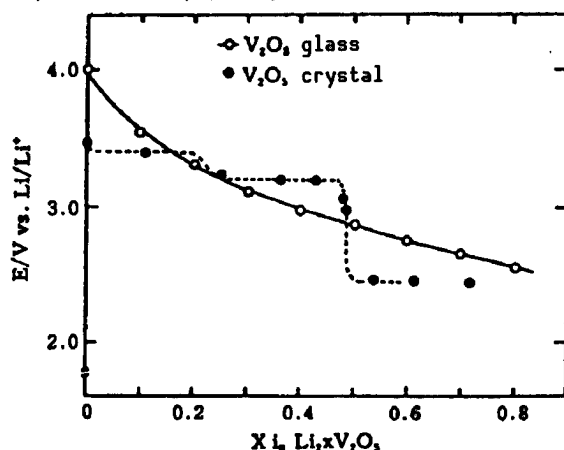
Figure 15. Open-Ended Voltage in
$Li/1M$ $LiClO_4$–PC/V_2O_5 Battery
(Cited from Ref. 43 material)
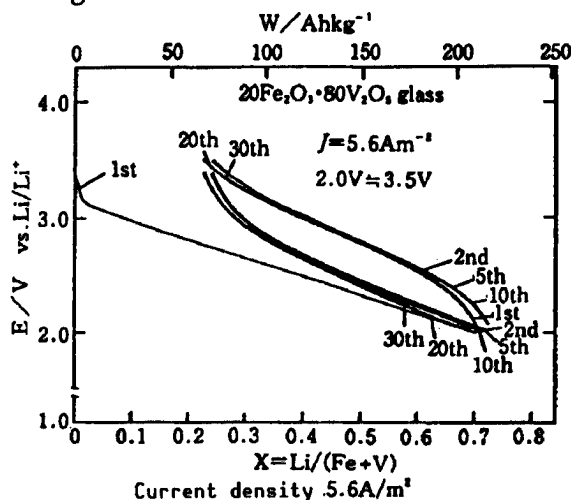
Figure 16. Discharge/Recharge Cycle
Characteristics in $Li/1M$ $LiClO_4$–PC/
$CuO \cdot 20Fe_2O_3 \cdot 80V_2O_5$ Glass
(Cited from Ref. 44 material)

Figure 15[43] compares the open-ended voltages between a V_2O_5 glass battery and a V_2O_5 crystal battery. A feature common to these batteries is that they have high electromotive force exceeding 3 volts. In the crystal version battery, the characteristic curve displays a step-mode change when the injected amount of Li^+ ions changes, while in the glass version, the curve exhibits smooth change. It is reported that the glass version has a considerably higher discharge capacity.

Figure 16[44] gives the discharge/recharge characteristics in the battery that uses $20Fe_2O_3 \cdot 80V_2O_5$ glass in the positive electrode at a current density of 5.6 A/m^2. The x-axis indicates both the ratio of intercalated Li^+ ions against the total metal atom volume within the glass and the discharge capacity. Though the output voltage deteriorates gradually with advancement of discharge/recharge cycle, the battery has favorable discharge/recharge characteristics. From these results, it can be seen that the glass is a promising candidate for use in the cathode of secondary lithium batteries.

This paper has described the creation of ultra-ion-conductive glass, the features of the glass, the conduction mechanism, the structure, and the application fields of the glass.

A special supplement combining 14 papers on ion-conductive glass, edited by this author, has been published in the JOURNAL OF MATERIALS CHEMISTRY AND PHYSICS.[45] I am grateful if these papers are of any help in furthering research on ion-conductive glass.

References

1. Minami, T., CHEMISTRY, Vol 38, 1983, p 412.

2. Kido, T. and Fueki, E., "Solid-State Ionics," Kodansha Publishing Co., 1986.

3. Minami, T., Takuma, Y., Tanaka, M., J. ELECTROCHEM. SOC., Vol 124, 1977, p 1659.

4. Minami, T., J. NON-CRYST. SOLIDS, Vol 95/96, 1987, p 107.

5. Minami, T., Ceramic Data Book '85 (compiled by a ceramic data book publishing committee), Industrial Product Technology Association, 1985, p 373.

6. Minami, T., Nambu, H., and Tanaka, M., J. AM. CERAM. SOC., Vol 60, 1977, p 467.

7. Minami, T., Ikeda, Y., and Tanaka, M., J. NON-CRYST. SOLIDS, Vol 52, 1982, p 159.

8. Minami, T., Imazawa, K., and Tanaka, M., Ibid., Vol 42, 1980, p 469.

9. Wada, H., Menetrier, M., Levasseur, A., and Hagenmuller, P., MAT. RES. BULL., Vol 18, 1983, p 189.

10. Robert, G., Malugani, J.P., and Saida, S., SOLID STATE IONICS, Vol 3/4, 1981, p 311.

11. Souquet, J.L., Robinel, E., Barrau, B., and Ribes, M., Ibid., p 317.

12. Levasseur, A., Cales, B., Reau, J.M., and Hagenmuller, P., MAT. RES. BULL., Vol 13, 1978, p 205.

13. Miyauchi, K., Matsumoto, K., Kanehori, K., and Kudo, T., SOLID STATE IONICS, Vol 9/10, 1978, p 1469.

14. Miyauchi, K., Matsumoto, K., Kanehori, K., and Kudo, T., ELECTROCHEMIS-TRY, Vol 51, 1983, p 211.

15. Liu, C. and Angell, C.A., SOLID STATE IONICS, Vol 13, 1984, p 105.

16. Machida, N. and Minami, T., J. AM. CERAM. SOC., Vol 71, 1988, p 784.

17. Susman, S., Delbecq, C.J., McMillan, J.A., and Roche, M.F., SOLID STATE IONICS, Vol 9/10, 1983, p 667.

18. Hunter, C.C. and Ingram, M.D., Ibid., Vol 14, 1984, p 31.

19. Minami, T., J. NON-CRYST. SOLIDS, Vol 73, 1985, p 273.

20. Kanno, R., Takeda, Y., Kanemura, T., and Yamamoto, O., MAT. RES. BULL., Vol 19, 1984, p 999.

21. Minami, T. and Yamen, A., CHEM. EXPRESS, Vol 1, 1986, p 567.

22. Hong, H.Y-P., MAT. RES. BULL, Vol 13, 1978, p 117.

23. Alpen, U.V., Bell, M.F., and Wickelhaus, W., J. ELECTROCHIM. ACTA, Vol 23, 1978, p 1395.

24. Hu, Y-W., Raistrick, I.D., and Huggins, R.A., J. ELECTROCHEM. SOC., Vol 124, 1977, p 1240.

25. Yamamoto, T., Takeda, Y., and Sugano, R., CHEMISTRY, Vol 30, 1983, p 387.

26. Glass, A.M., Lines, M.E., Nassau, K., and Shiever, J.W., APPLY. PHYS. LETT., Vol 31, 1977, p 249.

27. Tatsumisago, M., Minami, T., and Tanaka, M., J. AM. CERAM. SOC., Vol 64, 1981, p C-97.

28. Tatsumisago, M., Hamada, A., Minami, T., and Tanaka, M., Ibid., Vol 65, 1982, p 575.

29. Tatsumisago, M. and Minami, T., MAT. CHEM. PHYS., Vol 18, 1987, p 1.

30. Tatsumisago, M., Minami, T., and Tanaka, M., GLASTECH. BER., Vol 56K, 1983, p 945.

31. Tatsumisago, M., Machida, N., and Minami, T., J. CERA. SOC. JPN., Vol 95, 1987, p 197.

32. Wapenaar, K.E.D. and Schoonman, J., J. ELECTROCHEM. SOC., Vol 126, 1979, p 667.

33. Glass, A.M., J. APPL. PHYS., Vol 51, 1980, p 3756.

34. Ravaine, D. and Souquet, J.L., PHYS. CHEM. GLASSES, Vol 18, 1977, p 27.

35. Minami, T., Matsuda, K., and Tanaka, M., SOLID STATE IONICS, Vol 3/4, 1981, p 93.

36. Minami, T. and Tanaka, M., J. NON-CRYST. SOLIDS, Vol 38/39, 1980, p 289.

37. Huggins, R.A., In "Diffusion in Solids," (Nowick, A.S. Burton, J.J., ed)., Academic press, New York, Chapter 9, 1975.

38. Liu, C., Sundar, H.G.K., and Angell, C.A., SOLID STATE IONICS, Vol 18/19, 1986, p 442.

39. Minami, T., Katsuda, T., and Tanaka, M., J. NON-CRYST. SOLIDS, Vol 29, 1978, p 389.

40. Malugani, J.P. and Mercier, R., SOLID STATE IONICS, Vol 13, 1984, p 293.

41. Malugani, J.P., Mercier, R., and Tachez, M., Ibid., Vol 21, 1986, p 131.

42. Machida, N., Sakono, I., Tatsumisago, M., and Minami, T., CHEM. LETT., 1985, 1501.

43. Machida, N., Fuchida, R., and Minami, T., J. ELECTROCHEM. SOC., Vol 136, 1989, p 2133.

44. Ibid., Vol 137, (1990, to be published).
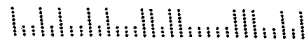
45. MAT. CHEM. PHYS., Vol 23, 1989, p 1.

— END —

Foreign Broadcast Information Service (FBIS) and Joint Publications Research Service (JPRS) publications contain political, military, economic, environmental, and sociological news, commentary, and other information, as well as scientific and technical data and reports. All information has been obtained from foreign radio and television broadcasts, news agency transmissions, newspapers, books, and periodicals. Items generally are processed from the first or best available sources. It should not be inferred that they have been disseminated only in the medium, in the language, or to the area indicated. Items from foreign language sources are translated; those from English-language sources are transcribed. Except for excluding certain diacritics, FBIS renders personal names and place-names in accordance with the romanization systems approved for U.S. Government publications by the U.S. Board of Geographic Names.

Headlines, editorial reports, and material enclosed in brackets [ ] are supplied by FBIS/JPRS. Processing indicators such as [Text] or [Excerpts] in the first line of each item indicate how the information was processed from the original. Unfamiliar names rendered phonetically are enclosed in parentheses. Words or names preceded by a question mark and enclosed in parentheses were not clear from the original source but have been supplied as appropriate to the context. Other unattributed parenthetical notes within the body of an item originate with the source. Times within items are as given by the source. Passages in boldface or italics are as published.

SUBSCRIPTION/PROCUREMENT INFORMATION

The FBIS DAILY REPORT contains current news and information and is published Monday through Friday in eight volumes: China, East Europe, Central Eurasia, East Asia, Near East & South Asia, Sub-Saharan Africa, Latin America, and West Europe. Supplements to the DAILY REPORTs may also be available periodically and will be distributed to regular DAILY REPORT subscribers. JPRS publications, which include approximately 50 regional, worldwide, and topical reports, generally contain less time-sensitive information and are published periodically.

Current DAILY REPORTs and JPRS publications are listed in *Government Reports Announcements* issued semimonthly by the National Technical Information Service (NTIS), 5285 Port Royal Road, Springfield, Virginia 22161 and the *Monthly Catalog of U.S. Government Publications* issued by the Superintendent of Documents, U.S. Government Printing Office, Washington, D.C. 20402.

The public may subscribe to either hardcover or microfiche versions of the DAILY REPORTs and JPRS publications through NTIS at the above address or by calling (703) 487-4630. Subscription rates will be provided by NTIS upon request. Subscriptions are available outside the United States from NTIS or appointed foreign dealers. New subscribers should expect a 30-day delay in receipt of the first issue.

U.S. Government offices may obtain subscriptions to the DAILY REPORTs or JPRS publications (hardcover or microfiche) at no charge through their sponsoring organizations. For additional information or assistance, call FBIS, (202) 338-6735,or write to P.O. Box 2604, Washington, D.C. 20013. Department of Defense consumers are required to submit requests through appropriate command validation channels to DIA, RTS-2C, Washington, D.C. 20301. (Telephone: (202) 373-3771, Autovon: 243-3771.)

Back issues or single copies of the DAILY REPORTs and JPRS publications are not available. Both the DAILY REPORTs and the JPRS publications are on file for public reference at the Library of Congress and at many Federal Depository Libraries. Reference copies may also be seen at many public and university libraries throughout the United States.